

A physics-based approach to flow control using system identification

Aurelien Hervé¹, Denis Sipp¹, Peter J. Schmid^{2†} and Manuel Samuelides³

¹ ONERA - The French Aerospace Lab, 8 rue des Vertugardins, 92190 Meudon, France

² Laboratoire d'Hydrodynamique (LadHyX), CNRS-Ecole Polytechnique, 91128 Palaiseau, France

³ ONERA - The French Aerospace Lab, 2 av. Edouard Belin, 31055 Toulouse, France

(Received 1 April 2011; revised 9 December 2011; accepted 23 February 2012;
first published online 7 June 2012)

Control of amplifier flows poses a great challenge, since the influence of environmental noise sources and measurement contamination is a crucial component in the design of models and the subsequent performance of the controller. A model-based approach that makes *a priori* assumptions on the noise characteristics often yields unsatisfactory results when the true noise environment is different from the assumed one. An alternative approach is proposed that consists of a data-based system-identification technique for modelling the flow; it avoids the model-based shortcomings by directly incorporating noise influences into an auto-regressive (ARMAX) design. This technique is applied to flow over a backward-facing step, a typical example of a noise-amplifier flow. Physical insight into the specifics of the flow is used to interpret and tailor the various terms of the auto-regressive model. The designed compensator shows an impressive performance as well as a remarkable robustness to increased noise levels and to off-design operating conditions. Owing to its reliance on only time-sequences of observable data, the proposed technique should be attractive in the design of control strategies directly from experimental data and should result in effective compensators that maintain performance in a realistic disturbance environment.

Key words: flow control

1. Introduction

It is generally acknowledged that the targeted manipulation of fluid flow holds great promise for a wide range of technological and industrial applications. The enhancement of mixing, the suppression of instabilities, increasing the robustness to uncertainty and noise, the reduction of drag and the improvement of energy conversion efficiencies are but a few objectives that could be reached by employing flow control techniques. For this reason, the discipline of flow control has seen a distinct and steady rise within the fluid dynamics community and has generated interest in academia and industry alike. The majority of successful flow control applications are numerical in nature, where the environmental conditions are favourable to the control strategy or can be managed easily. Less success must be reported for the application of control laws to a disturbance environment typically encountered in physical experiments.

† Email address for correspondence: peter@ladhyx.polytechnique.fr

The success or shortfall of control strategies depends on many factors, principally among them the nature of the inherent flow dynamics. Noise amplifiers which are highly sensitive to the external disturbance environment pose great challenges to the design process. In this case, sources of noise and inaccuracies have to be captured or modelled accurately, since they form the basis of the observed unsteadiness of the flow (Bagheri, Brandt & Henningson 2009). Noise amplifiers are ubiquitous in many engineering applications, such as separated flows, jets or boundary layers, to name a few. A quintessential and much-studied noise-amplifier flow is that over a backward-facing step of Barkley, Gomes & Henderson (2002) at $Re = 500$ where the unsteady behaviour originates from a bounded region of convective instability (Blackburn, Barkley & Sherwin 2008; Marquet *et al.* 2008).

Oscillator flows, on the other hand, are characterized by the presence of a global instability and are by nature insensitive to the ambient disturbance environment as well as to modelling inaccuracies. Suppression of global instabilities (e.g. von-Kármán vortex streets or the shear layer forming over an open cavity) within the linear regime thus puts markedly less stringent constraints on modelling the external disturbance environment (Cattafesta *et al.* 2003; Samimy *et al.* 2003, 2007; Barbagallo, Sipp & Schmid 2009; Ma, Ahuja & Rowley 2010; Sipp *et al.* 2010), but raises different issues related to nonlinear saturation of global instabilities. Besides the intrinsic flow behaviour, the control design approach further divides the techniques and strategies necessary for a successful manipulation of fluid flows. Two approaches have to be distinguished: a model-based approach and a system-identification approach. In the former, a model that accurately describes the flow behaviour is derived *a priori* from the known flow physics. While for simple to moderately complicated geometries and/or artificial disturbance environments this approach has been quite successful, modelling difficulties increasingly arise as the flow becomes more complex and the disturbance environment becomes more realistic. Moreover, coherent fluid structures such as proper orthogonal decomposition (POD) modes, global modes or balanced modes play an important role in the Galerkin-based model-reduction step of the flow design process (see Efe & Ozbay 2003; Rowley, Colonius & Murray 2004; Akervik *et al.* 2007; Barbagallo *et al.* 2009; Sipp *et al.* 2010). The alternative system-identification approach does not rely on a physical model, but rather establishes an approximate relation between input and output signals directly from their observations over time (Ljung 1999). In this sense, system identification is a data-based technique. In most applications of system-identified control design (see Huang & Kim 2008 for an application to flow separation control), the identification process is used as a black-box technique, i.e. with little regard to a proper motivation of its parameters or a physical interpretation of its outcome.

Independently of the chosen control design technique, a reduction of the prescribed or identified model is often necessary. For control applications, recent studies have conclusively shown that balanced modes yield efficient reduced-order models on which a controller can be based (Moore 1981; Rowley 2005; Barbagallo *et al.* 2009). A model can be computed directly from the projection of the governing equations onto a basis that uses snapshots of the flow (Rowley 2005; Barbagallo *et al.* 2009) or from a realization of the observed dynamics (Juang & Pappa 1985; Akers & Bernstein 1997; Gibson, Lee & Wu 2000; Ma *et al.* 2010). Both techniques will ultimately lead to the same reduced-order model, expressed on the balanced basis.

The aim of this study is the introduction of a system-identification technique to a flow control problem and its link with a classical model-based control design process for the effective manipulation of noise-amplifier flows. In particular, during

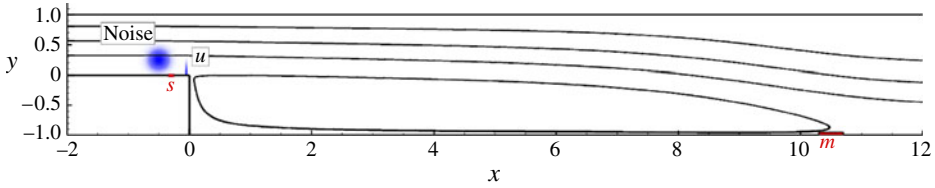


FIGURE 1. (Colour online available at journals.cambridge.org/flm) Sketch of flow geometry, including the different inputs and outputs. Two skin-friction measurements, s and m , are taken, respectively, at the top of the backward-facing step and at the end of the recirculation bubble. The control input u is given by the amplitude of actuation, composed of a spatial, Gaussian distribution of vertical velocity. The upstream forcing is introduced via a similar, spatially localized forcing, but with a stochastic amplitude w . The streamlines illustrate the mean flow \mathbf{v}_0 .

the identification phase we are interested in a rigorous interpretation of parameter choices and the physical understanding and role of various terms of the identified model.

We rely on linear systems theory that states that a model can be designed that recovers the perturbation dynamics from observable inputs. This model will furthermore benefit from the specifics of our configuration and control setup. A general equation with a physically motivated coefficient structure can thus be defined, and system identification techniques will determine these coefficients by a fitting algorithm to available data. Once the model is identified, a state–space optimal controller will be designed.

The article follows the following outline. The flow configuration and model equations are introduced in § 2, after which a brief review of classical Galerkin-based methods for the design of LQG-controllers is given, along with a general introduction of system identification (§ 3). This survey also addresses limitations of the Galerkin approach and helps motivate our alternative procedure. The design procedure of an ARMAX (auto-regressive moving-average exogenous) model based solely on observable data is presented in § 4; a physical interpretation of the model and its coefficients is given, before it is compared to the classical Galerkin-derived Kalman estimator. The subsequent control design process is the topic of § 5, where the compensator is designed, and applied to numerical simulations of the flow. The performance and robustness to noise of the compensator obtained are critically assessed. Conclusions and a summary of the most relevant results are offered in the final section (§ 6).

2. Configuration and governing equations

2.1. Noise amplifier over a backward-facing step

The configuration studied in this article consists of a two-dimensional backward-facing step that has previously been used, e.g. in Barkley *et al.* (2002). Variables are non-dimensionalized using the step height and the upstream centreline velocity; based on these values, the Reynolds number is chosen as $Re = 500$. The computational domain is taken as $(x, y) \in [-10, 50] \times [-1, 1]$ and is partially sketched in figure 1. The upstream boundary condition is modelled by an inflow of Poiseuille type; the upper and lower boundaries are set to wall conditions $\mathbf{v}_{tot} = 0$. For the chosen Reynolds number of $Re = 500$, the above flow configuration is globally stable. Nevertheless, the

flow exhibits a convective instability along the shear layer extending from the top of the step (at $x = 0$, location of branch I) to about $x = 25$ (branch II). As reported in Blackburn *et al.* (2008), the resulting flow unsteadiness is due to this local region of convective instability which is contained between upstream and downstream regions of stability. Even though a global stability analysis does not produce unstable global modes, transient growth of perturbations along the shear layer may arise due to the non-normality of the linearized Navier–Stokes operator. Generic fluid behaviour of this type is an example of a *noise amplifier*: a globally stable flow that still shows a significant, spatially localized response to an external disturbance environment.

The control of our flow configuration is aimed at reducing flow unsteadiness, which is quantified by the energy of the perturbations. As this energy is not easily observable in a real system, a skin-friction measurement m_{tot} is introduced at a downstream position. The sensor is located near the end of the first recirculation bubble at $x = 10.5$ (see figure 1), and $m_{tot}(t)$ will cease to fluctuate as the bubble is stabilized by our control effort. The fluctuating part of the measurement m_{tot} can therefore be taken as our control objective, which is to be minimized; it is then expected that the same control also reduces the global energy of the perturbations.

The external perturbations that will amplify along the shear layer and then impact on the objective m_{tot} originate within the upstream boundary layer. An upstream sensor s_{tot} is placed at $x = -0.3$ and will be used as an input to the compensator. If the sensor s_{tot} is sufficiently sensitive to the external perturbations, its measurements will provide important information about the effects of noise on the system.

For clarity, we introduce the notation of an underline denoting a quantity that is neither known nor measurable in a realistic environment. Generally speaking, a precise knowledge of the underlined quantities is required in a Galerkin-based model reduction approach while they will not be used during the control design process based on system identification.

We consider the dynamics of the flow field \mathbf{v}_{tot} driven by an external forcing term of the form $\underline{\mathbf{F}}_w w(t)$. This term stands for upstream unknown forcings which sustain unsteadiness in the flow field: $w(t)$ is a random forcing of standard deviation $\underline{\sigma}_w$ while $\underline{\mathbf{F}}_w$ is the spatial structure, which is of Gaussian shape

$$\underline{\mathbf{F}}_w(x, y) = \underline{\mathbf{A}} \exp\left(\frac{-(x - x_0)^2}{2\underline{\sigma}_x^2}\right) \exp\left(\frac{-(y - y_0)^2}{2\underline{\sigma}_y^2}\right). \quad (2.1)$$

The control action will be given by a term of the form $\underline{\mathbf{F}}_u u(t)$. The spatial structure $\underline{\mathbf{F}}_u$ consists of a similar Gaussian momentum forcing (although of smaller spatial extent) which is located at the top of the backward-facing step and driven by the scalar control law $u(t)$ which is yet to be determined. The control term will introduce a forcing at the upstream edge of the convectively unstable region; a small control should thus substantially affect the system and have a noticeable impact on the objective m_{tot} .

The spatial characteristics of both momentum forcing terms are defined by the coefficients in table 1; the momentum forcing terms are also sketched in figure 1. The velocity field expressed in Cartesian coordinates $\mathbf{v}_{tot} = [u_{tot} \ v_{tot}]^T$ is governed by the following non-dimensional equations:

$$\nabla \cdot \mathbf{v}_{tot} = 0, \quad (2.2a)$$

$$\partial_t \mathbf{v}_{tot} + \mathbf{v}_{tot} \cdot \nabla \mathbf{v}_{tot} = -\nabla p_{tot} + \frac{1}{Re} \Delta \mathbf{v}_{tot} + \underline{\mathbf{F}}_w w(t) + \underline{\mathbf{F}}_u u(t), \quad (2.2b)$$

	\underline{x}_0	\underline{y}_0	$\underline{\sigma}_x$	$\underline{\sigma}_y$	\underline{A}
Noise	-0.5	0.25	0.1	0.1	4.0
Control	-0.05	0.01	0.01	0.1	4.0

TABLE 1. Parameters that define the spatial Gaussian distributions of the control and noise source.

$$s_{tot} = \int_{x=-0.35}^{x=-0.25} \partial_y v_{tot} dx, \quad m_{tot} = \int_{x=10.5}^{x=10.7} \partial_y v_{tot} dx. \quad (2.2c)$$

In the following, we will consider small noise amplitudes $\underline{\sigma}_w \ll 1$. All quantities will fluctuate around their means, which will be denoted by a subscript zero. Let us explicitly introduce the fluctuations given by $\mathbf{v}_{tot} = \mathbf{v}_0 + \mathbf{v}$, $\mathbf{p}_{tot} = \mathbf{p}_0 + \mathbf{p}$, $m_{tot} = m_0 + m$ and $s_{tot} = s_0 + s$. Since the flow is a noise amplifier, the amplitude of all fluctuations \mathbf{v} , \mathbf{p} , m , s but also u scale with $\underline{\sigma}_w$. The flow field \mathbf{v}_0 corresponds to a base flow, i.e. a steady solution of the nonlinear Navier–Stokes equations. After introducing these expressions into (2.2) the dominant order cancels out and we arrive at the following equations that govern the fluctuating part of the flow field:

$$\nabla \cdot \mathbf{v} = 0, \quad (2.3a)$$

$$\partial_t \mathbf{v} + \mathbf{v} \cdot \nabla \mathbf{v}_0 + \mathbf{v}_0 \cdot \nabla \mathbf{v} = -\nabla p + \frac{1}{Re} \Delta \mathbf{v} + \underline{\mathbf{F}}_w w(t) + \underline{\mathbf{F}}_u u(t). \quad (2.3b)$$

This shows that the dynamics of the fluctuations around the mean flow is linear. In particular, the dynamics from the inputs ($w(t)$, $u(t)$) to the outputs ($s(t)$, $m(t)$) is linear. In an experiment, m and s are straightforwardly obtained by subtracting the mean measurements m_0 and s_0 from the actual measurements m_{tot} and s_{tot} .

Even though the controller will be designed and optimized for operation within a linear regime, results in § 5.2.3 will show a remarkable robustness of the control law with respect to nonlinear effects. For the design process, external excitations should remain as low as possible so that the system stays in the linear regime; but one can still expect to obtain good results with the computed controller as one ventures beyond its design point. This feature will also play a role from an experimental point of view, where a small-amplitude environment is used to design the control law which will remain applicable, with reasonable results, in a less quiet setting.

2.2. Numerical method

We use a direct numerical simulation code which solves the nonlinear, incompressible Navier–Stokes equations (2.2) in primitive variables (u_{tot} , v_{tot} , p_{tot}). To increase accuracy for low-amplitude perturbations, the code is based on the perturbed form (2.3) of the governing equations but still includes the nonlinear term ($\mathbf{v} \cdot \nabla \mathbf{v}$). Finite elements with a mesh composed of triangular elements are used for the spatial discretization; for our case, the mesh contains about 123 000 triangles. The velocity fields are projected onto six-node triangular elements with quadratic interpolation (P2-elements), while the pressure field is discretized using three-node triangular elements with linear interpolation (P1-elements). The pressure field is obtained using the Uzawa algorithm, preconditioned by the Cahouet–Chabart method (Glowinski 2003). The temporal discretization is semi-implicit and based on a second-order

backward-differentiation scheme. We use the standard free-outflow condition

$$p\mathbf{n} - Re^{-1}\nabla\mathbf{u} \cdot \mathbf{n} = 0 \quad (2.4)$$

at the outlet of our computational domain.

3. System identification for control-oriented flow modelling

In this section the model reduction based on Galerkin projections will first be briefly discussed, to motivate the use of identification methods in the design of optimal control strategies. In particular, we will focus less on its practical application but more on its underlying assumptions and requirements during the design process. *System identification* will then be introduced, as an alternative approach to model flow dynamics.

3.1. Model-based methods: Galerkin projection

A common method to obtain a reduced-order model is based on Galerkin projection. It consists of projecting the linearized Navier–Stokes equations onto a prescribed (bi-orthogonal) basis which results in a reduced state–space equation. The model must accurately represent the input–output behaviour of the full system; this prerequisite is a crucial component for the choice of bases that are appropriate for a given control application. POD bases (Efe & Ozbay 2003; Rowley *et al.* 2004; Barbagallo *et al.* 2009, and many others) which describe the most energetic structures of the system, or balanced bases (Moore 1981; Rowley 2005) which focus directly on the input–output behaviour of the system, are most commonly used to project the equations.

The Galerkin projection provides a linear dynamical model that is commonly expressed in standard finite-dimensional time-invariant state–space form. Projection of equations (2.3) onto the chosen basis yields

$$\mathbf{X}(t + 1) = \mathbf{A}\mathbf{X}(t) + \mathbf{B}u(t) + \mathbf{B}_w w(t), \quad (3.1a)$$

$$s(t) = \mathbf{C}_s \mathbf{X}(t) + g_m(t), \quad (3.1b)$$

$$m(t) = \mathbf{C}_m \mathbf{X}(t) + g_s(t). \quad (3.1c)$$

The variable \mathbf{X} is referred to as the state variable. It describes the amplitudes of the various spatial structures that have been taken as a projection basis. The plant noise, i.e. the random disturbance environment driving the state dynamics, is modelled by the term $\mathbf{B}_w w(t)$. It consists of the forcing source \mathbf{B}_w , which is driven by the stochastic scalar forcing term $w(t)$. The term \mathbf{B}_w captures the unknown external excitations that enter the system and stems from the projection of the spatial distribution $\underline{\mathbf{F}}_w$ of the forcing term onto the chosen basis. Analogously, the term $\mathbf{B}u(t)$ stands for the actuation: \mathbf{B} is obtained by projection of $\underline{\mathbf{F}}_u$ onto the Galerkin basis. The quantity (g_m, g_s) represents the noise sources for each of the two measurements. The temporal standard deviations of these stochastic quantities are inherent to the sensors (they are not determined by the projection) and are referred to as $\text{std}(g_m) = \underline{\mathbf{G}}_m$ and $\text{std}(g_s) = \underline{\mathbf{G}}_s$. The two matrices \mathbf{B} and \mathbf{B}_w describe system inputs in the form of forcing terms; the matrices $\mathbf{C}_{s,m}$ represent the extraction of information from the flow via the sensors (\mathbf{C} takes information from the state \mathbf{X}). The individual components of \mathbf{C} therefore refer to measurements of the spatial structures of the projection basis.

A Galerkin projection usually yields a continuous-time format for the state–space system (3.1). For simplicity we have chosen to formulate it in a discrete-time format, with t as the time step index. The remainder of the article pertaining to identification methods, it is more naturally expressed in the discrete-time framework. Yet, one

should keep in mind the equivalence of the continuous and discrete frameworks due to a straightforward transformation (see Antoulas 2005, for details on the correspondence between discrete and continuous-time matrices).

A proper model should accurately capture the transfer behaviour of the linear system from the input variables (w, u) to the output variables (s, m). The effectiveness of the model relies on the ability of the chosen Galerkin basis (e.g. POD modes, balanced POD modes, etc.) to represent this input–output mapping – a difficult undertaking in the light of the fact that the noise environment w is generally not known to a sufficient degree of detail (Dergham, Sipp & Robinet 2011). For this reason, simplifying assumptions about w (such as e.g. assuming it is spatially located) have to be made during the design process (see e.g. Bagheri *et al.* 2009), and their adverse impact on the overall performance of the compensated system has to be acknowledged as a deficiency of Galerkin-based control design. We would like to stress at this point that in the subsequent analysis a forcing w in the form of white noise is not required. Yet, it covers the most general case as it generates time-coloured fluctuations in s and m , which are the only quantities that are processed during the identification phase; the noise term w , on the other hand, never enters the analysis and is merely used to generate the perturbations.

3.1.1. Kalman filter

Computing the control law requires real-time knowledge of $X(t)$ which is commonly not available under realistic conditions. For this reason, an estimator that uses only partial information of the system to estimate an approximate state \hat{X} is used in lieu of X . The Riccati equation for the estimator depends on $(\mathbf{A}, \mathbf{B}_w, \mathbf{C}_s)$ and the signal-to-noise ratio σ_w/\mathbf{G}_s . The better the sensor, the lower \mathbf{G}_s ; the higher σ_w/\mathbf{G}_s , the more accurate the estimator.

The estimator consists of a dynamical system that recaptures the effect of noise sources w from the measurement(s) (in our case, the signal s) via a Kalman filter \mathbf{L} . The dynamics of the system has to be known such that the unknown forcing terms and their action on the entire flow field can be estimated. If the perturbations are observable from the measurement s , the optimal estimator reads

$$\hat{X}(t+1) = \underbrace{(\mathbf{A} - \mathbf{L}\mathbf{C}_s)}_{\mathbf{A}_e} \hat{X} + \mathbf{B}u + \mathbf{L}s, \quad (3.2a)$$

$$\hat{m} = \mathbf{C}_m \hat{X}. \quad (3.2b)$$

It statistically minimizes the error $\|\hat{X} - X\|_2$ (with \hat{X} as the estimated state) in order to provide an accurate prediction \hat{m} of the measurement m . Equation (3.2) illustrates that the effects of the stochastic field $\mathbf{B}_w w(t)$ are captured by processing the difference between the actual measurement s and the measurement $\mathbf{C}_s \hat{X}$ predicted by the model.

3.1.2. Assessment and limitations of Galerkin-based methods

Galerkin models are a popular choice for model reduction, owing to their ease of use in feedback applications, mathematical bounds on their convergence, and their link to physically relevant flow structures. But despite their widespread use, Galerkin-based methods for the computation of reduced-order models also suffer from notable limitations and drawbacks.

An accurate large-scale model of the state dynamics is required. The Galerkin projection requires that the flow dynamics is accurately represented by a physics-based model. The implementation of boundary conditions, the computation of the base flow,

the incorporation of turbulence effects via a model and the influence of neglected nonlinear effects have to be justified with due caution, and their influence on the final model has to be assessed carefully.

Observability of the basis is required. To accurately reproduce the input–output dynamics of the system, the projection basis has to be sufficiently observable. This requirement commonly necessitates the use of adjoint simulations to determine a balanced basis which, in turn, is mandatory for large-scale state models. If no adjoint simulations are at hand and only POD modes are used for the projection basis, then the resulting transfer function may only poorly reproduce the original one.

An explicit description of the actuator is difficult to obtain. To define \mathbf{B} , the spatial distribution $\underline{\mathbf{F}}_u$ of the actuator momentum forcing has to be known or estimated, which is problematic in any experimental application. If $\underline{\mathbf{F}}_u$ is not known, a technique discussed in Samimy *et al.* (2003) and Cattafesta *et al.* (2003) can be used. A Galerkin projection of the Navier–Stokes equations onto e.g. a POD basis then yields an autonomous set of ordinary differential equations. The influence of the external actuation hence appears implicitly which causes problems for the control design. In order to obtain an explicit description of the actuation, separation methods may be employed (see Efe & Ozbay 2003, for a complete description of the separation method) in addition to the reduced-order model computation.

A reduced-order model that accurately captures the influence of the upstream noise $w(t)$ on the state is difficult to obtain. To allow an accurate reduction of the dynamics, knowledge about the noise source is required when computing the reduction basis. In the absence of this knowledge, modelling assumptions have to be made (Bagheri *et al.* 2009; Dergham *et al.* 2011) or a full state-to-sensor mapping has to be determined. Either approach is problematic and has significant consequences for the overall performance and robustness of the compensator.

Statistical information about the external noise sources is necessary. The computation of the estimator (that is, the Kalman gain \mathbf{L}) requires at least an approximate knowledge of the spatial distribution of the external disturbance environment ($\underline{\mathbf{F}}_w$). Since statistical properties of the external forcing are often unknown or difficult to obtain, the estimator will ultimately perform suboptimally, leading to disappointing results when applied under realistic (experimental) condition.

3.2. An alternative approach: system identification

In this article we propose and apply an algorithmic process for the design of a controller based on a low-dimensional model that only requires data which can readily be extracted, for example, from a real lab experiment. This process relies on techniques from *system identification*, which provides quantitative information about the system’s dynamics directly from its observation. System identification provides models that are particularly well-suited for control applications since, by design, the only dynamics that are taken into account are part of the observable input–output behaviour of the system.

3.2.1. Predicting the effect of the observable sources

In general, the physical inputs of the flow are the control u and an *a priori* unknown number of external forcing sources w_k . The sources, whose effect can be detected by s before they reach m , are referred to as *predictable*, whereas the sources, which impact on m without having been detected by s , are referred to as *unpredictable*. Assuming linear flow behaviour, the output measurement m is given as a linear combination of

influences stemming from those sources

$$m = f_u u + \sum_{\text{predictable } w_k} f_{w_k} w_k + \sum_{\text{unpredictable } w_k} f_{w_k} w_k. \quad (3.3)$$

For all predictable forcing sources, a model can then be derived that aims at estimating the future measurement m by using the upstream measurement s according to

$$m = f_u u + f_s s + E, \quad (3.4a)$$

$$E = \sum_{\text{unpredictable } w_k} f_{w_k} w_k. \quad (3.4b)$$

In effect, this approach anticipates the effect of the predictable sources w_k on m by measuring their effect on the upstream sensor s before reaching m . What is not measurable by s cannot be anticipated and is included in an error term E . If the effect of the predictable forcing sources is well-estimated, a control law can be computed to cancel their influence on the measurement m . This approach is consistent with the Galerkin state–space framework introduced in § 3.1, since (f_s, f_u) defines a model that is equivalent to the estimator (or Kalman filter) given in (3.2). In particular, we note that these models share the same inputs/outputs. It is however important to bear in mind that the identified transfer function f_u is related to (3.2) rather than (3.1), and is therefore based on the system matrix $(A - \mathbf{L}\mathbf{C}_s)$ rather than A .

The system-identification approach aims at modelling the (f_s, f_u) transfer functions by a direct observation of the flow behaviour whereas the classical Galerkin approach derives them from the Navier–Stokes equations. Even though the two approaches differ, both aim to ultimately represent the dynamics that relate the available input(s) to the output(s) of the system. As pointed out by Kim & Bewley (2007), those dynamics are the only ones needed for a control-oriented low-order model.

It is important to realize that the model error referred to above arises from the part of the flow dynamics that cannot be predicted by the upstream sensor s . Consequently, term E will generally not be white Gaussian noise. As most of the linear identification methods commonly determine a model by assuming the unobservable dynamics as white-noise perturbations, this fact will raise important modelling issues. Most identified linear models (such as e.g. the subspace or ARX models, used by Huang & Kim 2008) assume E as white noise; they are referred to as *purely linear* by Ljung (1999), as they solve a least-squares error problem to determine the dynamics of the model. In contrast, a *pseudo-linear* ARMAX model will be introduced in § 4.1. It consists of a linear equation, computed via a nonlinear algorithm, hence allowing modelling of E as time-coloured noise (without any *a priori* knowledge of the colour of this noise).

3.2.2. Pseudo-experimental setup

One aim of our study is the introduction and assessment of low-order control design based on system identification that is adoptable for later applications to physical experiments. In view of this goal we will treat our numerical experiments in a quasi-experimental setting and process only data that would be easily available or measurable in reality. We will therefore impose a few restrictions on the design process. We will not require exact or approximate information about generally unknown quantities and in particular about all underlined quantities – for example, the characteristics of the upstream noise environment ($\underline{\mathbf{F}}_w, \underline{\sigma}_w$) and the behaviour of the actuator ($\underline{\mathbf{F}}_u$). This is in stark contrast to a (model-based) Galerkin approach

which necessitates the approximation, estimation or modelling of the external noise environment and the details of the actuation process. In addition, following a typical setup in a laboratory experiment, we will assume that upstream noise sources are omnipresent during the design procedure. It is thus not possible to process information where e.g. the control is the only source of external forcing. Also, we will allow sensors s and m to be corrupted by white measurement noise characterized by the standard deviations $\underline{\mathbf{G}}_s$ and $\underline{\mathbf{G}}_m$ whose precise values will also be considered as unknown in the design process. Finally, when controlling the flow, continuous control laws will have to be used. Although an impulse response of a linear system would provide a complete description of its transfer function, we assume that such an excitation is experimentally not feasible to a sufficiently high degree of accuracy.

3.2.3. Limitations of system identification

Like any computational techniques, system identification suffers from limitations, and, for a fair comparison, we present some of the weaknesses associated with system-identification methods.

Nonlinearity. In contrast to model-based methods, system-identified linear models can present great challenges when nonlinearities are present. In our configuration, the identification is performed in a quiet environment that ensures linear dynamics. Once identified, the model can show remarkable performance when exposed to stronger perturbations (§ 5.2.3). However, the identification process has to be performed within a linear flow regime if satisfying results are to be obtained.

Stability. Most linear identification algorithms cannot guarantee stability of the resulting model, contrary to model-based linear systems. This issue becomes critical, if the system is excited by an unknown source that continuously affects the objective measurement. System identification may model such a sustained influence as an instability of the system, unaware of the fact that it stems from an unknown external excitation source. This matter will be investigated further in § 4.4 where such an additional forcing source will be considered. In contrast to *purely linear* models, a *pseudo-linear* model will be introduced in § 4.1 that ensures stability.

Objective functional. In contrast to a Galerkin-POD approach where the total energy of the flow can be estimated and taken as an objective function, system identification only allows the control of observable objectives. In this article we introduce a downstream sensor and presume that a successful reduction of the measured fluctuations will give rise to a proportional reduction of the global fluctuation energy. Such an assumption is, of course, not assured in general and needs to be verified *a posteriori*. Note also that, once the model is identified, the downstream measurement is no longer needed. The goal of the model/compensator is to predict and to cancel a detected perturbation before it reaches the downstream measurement. Owing to the convective nature of the flow, any information from downstream of the actuator is irrelevant since it is already out of reach of the controller. From an experimental point of view, this implies that the downstream sensor is only needed during the identification process. Unlike the upstream sensor, it does not have to be included in the controller.

Tuning the model. System identification can often require setting some parameters for the regression algorithm. Although these coefficients can be based on a physical interpretation (§ 4.1), it requires some insight to properly set them; the same is not necessary for the model-based approach.

4. ARMAX as a linear model to identify the backward-facing-step dynamics

In this section the ARMAX model will be presented. Its physical interpretations will be discussed in §4.1, and it will be used to model the backward-facing step (§4.2), before it is finally compared to the model that can be derived from a classical Balanced-POD Galerkin framework (§4.3). To assess the effect of the unpredictable forcing sources (equation (3.3)) on the identification process, an additional source of excitations has been used in the flow computation. Its location is chosen so that it corrupts the m signal without affecting s , in order to identify the dynamics in the presence of dynamics that are non-observable by s , but time coloured (§4.4). The performance of the ARMAX model in the presence of the additional forcing source will be compared to the performance of purely linear models.

4.1. Introduction of the ARMAX model and its physical interpretation

An auto-regressive moving-average exogenous (ARMAX) model will be used to identify the transfer function of the system. We have

$$m(t) + \underbrace{\sum_{k=1}^{n_a} a_k m(t-k)}_{\text{auto-regressive}} = \underbrace{\sum_{k=n_{du}}^{n_{bu}+n_{du}} b_k^u u(t-k)}_{\text{exogenous 1}} + \underbrace{\sum_{k=n_{ds}}^{n_{bs}+n_{ds}} b_k^s s(t-k)}_{\text{exogenous 2}} + E(t), \quad (4.1a)$$

$$E(t) = \underbrace{\sum_{k=1}^{n_c} c_k e(t-k)}_{\text{moving average}} + e(t). \quad (4.1b)$$

The superscripts u, s in (4.1) allow to differentiate two different sequences of (b_k) coefficients and should not be confused with an exponentiation. The regression consists of finding the (a_k, b_k, c_k) coefficients, such that the residual $e(t)$ only contains white noise of minimal variance.

The following parameters play an important role in the ARMAX-model: n_a is the number of previous outputs on which the current output depends (the Auto-Regressive part); the parameters n_{du}, n_{ds} denote the number of input samples that pass before the input starts to affect the output (i.e. measuring delay). Setting $n_d > 0$ means that the inputs do not have an instantaneous effect on the measurement, which is the case for our configuration. The parameters n_{bu}, n_{bs} signify the number of previous inputs on which the current output depends (the eXogenous part). For each input i , $n_{bi} + n_{di}$ defines the truncation order of the transfer function $i \rightarrow y$, where y is defined in (4.5) below (and the delay n_d causes the first coefficients $b_k^i, k = 0, \dots, n_{di} - 1$, to vanish). Finally, n_c is used to model time-coloured noise (the Moving-Average part). This term will be further discussed in §4.1.2.

4.1.1. Auto-regressive model

Equation (3.4a) involves two transfer functions that can be represented as

$$m(t) = \sum_{k=0}^{\infty} h_k \tilde{u}(t-k), \quad (4.2)$$

where

$$\tilde{u}(t) = \begin{bmatrix} u(t) \\ s(t) \end{bmatrix}. \quad (4.3)$$

The h_k coefficients are referred as the Markov parameters. They represent the impulse response of the system. When using the state–space Kalman estimator, these coefficients are defined as

$$h_k = \left[\mathbf{C}_m \mathbf{A}_e^k \mathbf{B} \quad \mathbf{C}_m \mathbf{A}_e^k \mathbf{L} \right] \quad (4.4)$$

where $\mathbf{C}_m, \mathbf{A}_e, \mathbf{L}$ are defined as in (3.2)

Since the dynamics of the model is stable, we have $\lim_{k \rightarrow \infty} h_k = 0$, and the transfer function can be approximated by truncating the h_k -sequence at some index N based on a given error bound ε , i.e. $|h_k| < \varepsilon$ for $k > N$. The minimum rank N for which the truncation gives accurate results can be rather high (especially for weakly damped systems) and requires the identification of a large number of Markov parameters. In an effort to reduce the number of parameters, an auto-regressive representation of the transfer function can be used as follows.

Since the measurement m stems from a continuous physical system dynamics, it is reasonable to assume a strong auto-correlation in time. Therefore, one can expect to find a set of coefficients $a_{k=1, n_a}$ that defines

$$y(t) = m(t) + \sum_{k=1}^{n_a} a_k m(t-k) \quad (4.5)$$

such that $|y(t)| \ll |m(t)|$ for all time. The variable y can be viewed as the residual of the auto-regression of m over n_a time steps; the stronger the auto-correlation of the signal m , the lower the residual norm $|y|$.

By defining the Markov parameters b_k of the transfer function $\tilde{u} \rightarrow y$ as

$$y(t) = \sum_{k=0}^{\infty} b_k \tilde{u}(t-k) \quad (4.6)$$

the relation $|y| \ll |m|$ together with (4.2) and (4.6) yields $|b_k| \ll |h_k|$ for all k , which means that the Markov parameters b_k converge towards zero faster than the original Markov parameters h_k do. It is thus possible to truncate the transfer function $\tilde{u} \rightarrow y$ at a lower order $N' < N$ without loss of accuracy. Equation (4.5) then yields

$$m(t) = - \sum_{k=1}^{n_a} a_k m(t-k) + \sum_{k=0}^{\infty} b_k \tilde{u}(t-k). \quad (4.7)$$

This expression is thus based on a significantly smaller set of coefficients (compared to the direct representation (4.2)) to describe the transfer function $\tilde{u} \rightarrow m$.

We observe that the representations (4.2) and (4.7) are mathematically equivalent. However, the truncation step for each of these sequences has different interpretations. Based on (4.2), a truncation at order N is equivalent to the statement that the system returns to its equilibrium state (the base flow) in N time steps after being excited by an impulse in \tilde{u} ; for a weakly damped noise amplifier, N can be large. When using the recursive equation (4.7), a truncation at order N' means that N' time steps are needed to describe how an impulse in \tilde{u} starts to disturb the flow. The remaining observed dynamics is described by the auto-regressive part and consists of a self-sustaining process. This latter description is more suited to our case, since we know that the dynamics arises from weakly damped self-sustained oscillations that are triggered by small upstream disturbances.

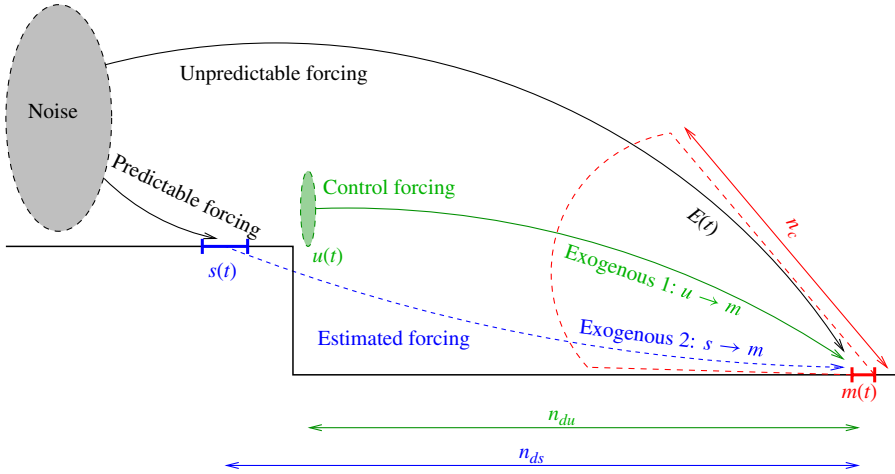


FIGURE 2. (Colour online) Schematic representation of the different terms and parameters in the ARMAX equation.

4.1.2. Exogenous and moving-average part

Figure 2 presents a sketch showing a physical interpretation of the ARMAX equation. The exogenous terms attempt to capture the effect of the two inputs on the output m , as shown by the arrows labelled Exogenous 1 and Exogenous 2. As the inputs do not instantaneously affect the output, they are delayed using the (n_{du}, n_{ds}) coefficients which can be linked to the convective speed of the flow.

Although the upstream sensor s succeeds in acquiring useful information about the external excitations, it is not sufficient to observe the full external forcing. For this reason, dynamical characteristics that stem from non-observable (by s) excitations will pass through the system to eventually reach the output m . As such dynamics cannot be predicted by our model, its overall effect on the measurement m will be observed as measurement error $E(t)$. This error term contains the effects of advected and selectively amplified excitations; thus, the measurement noise cannot be modelled as white noise. Huang & Kim (2008) attempted to model a generic separated flow using an ARX equation, which represents a special case of our ARMAX equation with $n_c = 0$, i.e. with white-noise residuals. Not surprisingly, the ARX model showed poor results, attributed to lacking robustness to measurement noise. In contrast to the ARX model, the moving average part of the ARMAX equation allows us to model the measurement error as time-coloured Gaussian noise. This term is a key feature of our approach, as it ensures robustness against time-coloured noise that arises from unobservable (by s) forcing terms that propagated through the system.

Once the ARMAX equation has been determined to estimate m with sufficient accuracy, the downstream sensor m can be eliminated, as the model – and consequently the controller – will only use s and u as inputs.

4.2. Designing the model

4.2.1. DNS datasets for learning and testing

The coefficients in the ARMAX model are computed by first performing a direct numerical simulation (DNS) employing an arbitrary forcing law u . The DNS uses a time step of $dt_{dns} = 0.002$, and the time interval between measurement samples

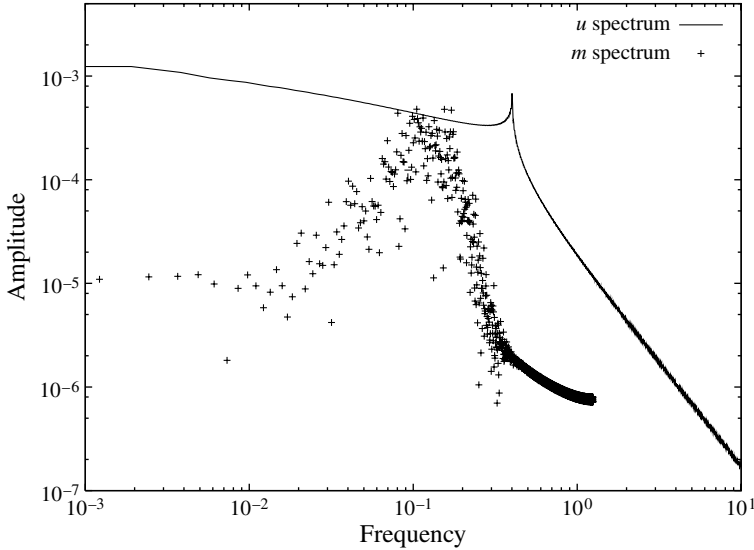


FIGURE 3. Comparison between the spectrum of the designed forcing signal u (taken for $t \in [0; 60]$ in figure 4b) and the spectrum of the measured signal m from an unforced, but noise-contaminated simulation.

is $dt_m = 0.1$. A (changing) pseudo-random noise is always introduced in the numerical simulations, which mimics upstream excitations of unknown source and distribution (as they are present in physical experiments). Unless otherwise stated, we will use in the following a low-amplitude forcing $\sigma_w = 0.01$, which ensures that the perturbations behave linearly, and perfect sensors characterized by $\underline{\mathbf{G}}_s = \underline{\mathbf{G}}_m = 0$.

The spectrum of the measurement $m(t)$ for the case of an unforced simulation (i.e. with $u = 0$, but with upstream excitations present) is plotted in figure 3 (crosses). It demonstrates that the bulk of the excited frequencies are located between 10^{-2} and 0.2 . We thus can assume that most of the flow dynamics can be excited by using a forcing law u that covers this frequency band. Figure 4 shows three signals, s , u , and m , that have been used as a learning dataset to identify the model. Of the three signals, s and m are not given *a priori* but are extracted from the DNS. The control law u is continuous in time (as required by an actuator in a real experiment) and designed to allow the simultaneous identification of the action of both u and s on the measurement m : the peaks in u trigger a similar but delayed response in m , while between the peaks (where the action of u is rather weak, e.g. from $t = 40$ to $t = 60$) the response of m to s can be identified. For comparison, the spectrum of the chosen forcing u is given in figure 3. The maximum amplitude of the forcing u has to be chosen such that its triggered response can be easily identified over the noisy perturbations; at the same time, it is limited by the fact that triggered nonlinear effects are undesirable for the identification process. A few representative snapshots of the perturbation vorticity are displayed in figure 5. It clearly illustrates transient spatial growth (from $x = 0$ to $x = 25$) arising from the forcing followed by exponential decay (for $x > 25$).

Two additional test datasets have been used (as shown in figure 6 and figure 7) to check if the identified model is able to reproduce the dynamics of m for different datasets. These two datasets provide a broader range of conditions to which the flow and the model are being exposed. Figure 6 shows the same control law u as the one

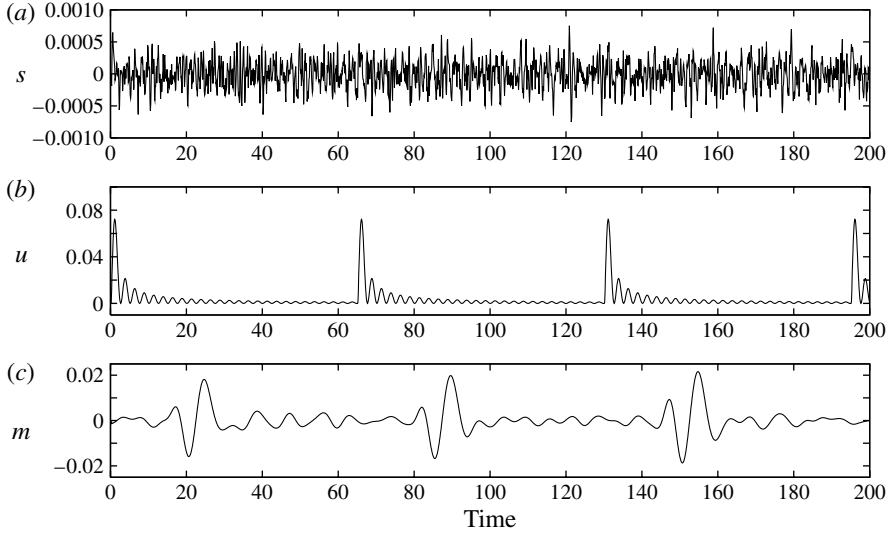


FIGURE 4. Three data sequences, used to identify the model: (a) the measurement s capturing the influence of external noise, (b) a deterministic, broadband control law u , (c) the measurement m taken near the reattachment point.

used in the previous dataset, whereas the upstream measurement s is subjected to a different noise source. This test is to ensure that the influence of u and s on m are identified independently. Figure 7 shows a different control law which corresponds to a step followed by an arbitrary combination of a small number of sinusoidal functions.

4.2.2. Choosing the ARMAX coefficients

The ARMAX regression introduced above requires the selection of the following coefficients: n_a , n_{bu} , n_{bs} , n_{du} , n_{ds} , and n_c . As explained in § 4.1.2, these coefficients are related to various properties of the flow and can thus be easily set. They should improve the regression efficiency but do not have to be defined precisely. In addition, the more data that are available for the identification process, the less important the exact values of these coefficients become.

In determining n_a , an auto-correlation of $m(t)$ has been calculated using one of the above datasets. Results are shown in figure 8(a): the solid curve corresponds to the auto-correlation. Owing to the short dataset, the auto-correlation should not be assumed as fully converged. Nevertheless, the correlation shows a quasi-oscillatory behaviour. We set $n_a = 36$ (indicated by the grey zone in figure 8(a) which approximately corresponds to half this oscillation period.

The time delays n_{du} , n_{ds} can be obtained by considering the cross-correlations between $[u(t)s(t)]$ and $m(t)$. Figure 8(b) displays the cross-correlation between u and m ; it shows that the influence of u is felt at the measurement location at $t \approx 11$. It was significantly more difficult to reach convergence of the cross-correlation between s and m , since the spectrum of s is substantially closer to a flat white-noise spectrum. An experimental setup would probably provide substantially longer datasets. This would allow us to determine these correlations with enough accuracy. In our study, however, we chose to evaluate the convective time scale of the flow in a different way. We note that the evaluation of n_{du} , n_{ds} can also be derived from an estimation of the convective speed of the flow. The convective speed of perturbations is approximately

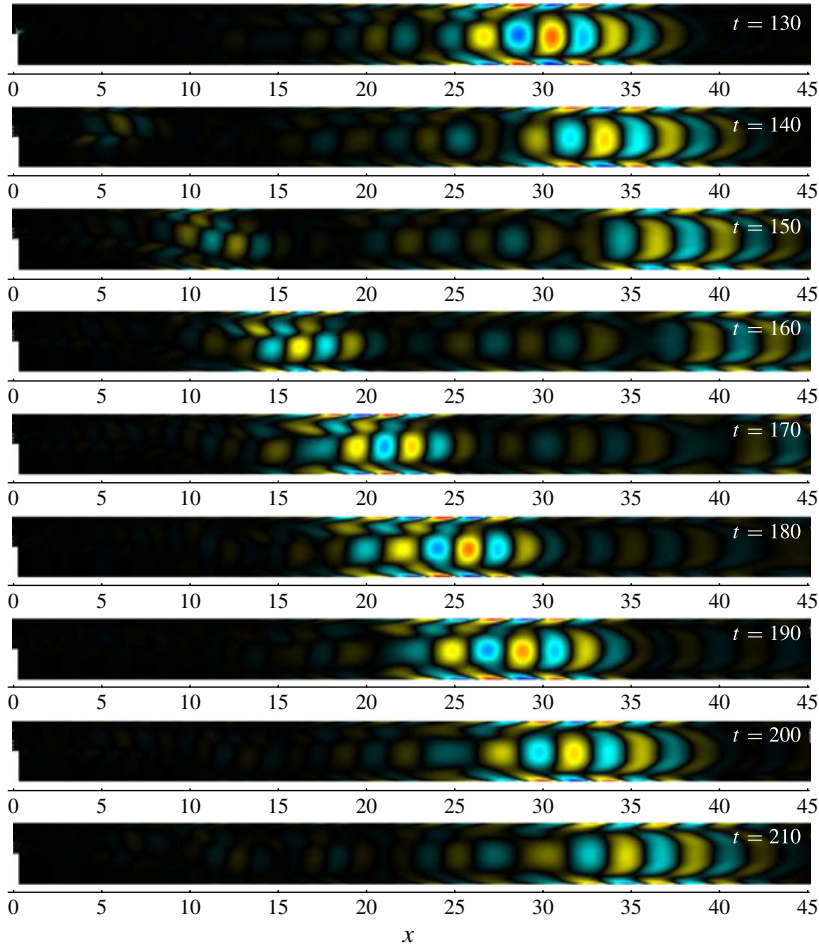


FIGURE 5. Contours of the perturbation vorticity for the simulation that produced the dataset in figure 4. The control (visible at $t = 130$) creates a wave packet that is spatially amplified between $x = 0$ and $x = 25$ before it exponentially decays. The effect of the control peak at $t \approx 70$ is still visible at $t = 130$ when the second control peak occurs. Between the two triggered wave packets, additional perturbations are visible which can be ascribed to excitations from the upstream noise.

given by the time until a particle released at the locations of s and u reaches the sensor location of m . Integrating a numerical simulation with passive particles, or simply the base-flow equations, will lead to the same results, as small perturbations will not significantly affect the convective speed of the flow. Since it is acceptable to underestimate the delays, but not to overestimate them, the fastest particle (initially located at the centreline position) is taken as a reference. Figure 9 shows different streamlines of the base flow, with passive particles being integrated from the actuator location (a) for determining n_{du} and the sensor location (b) for determining n_{ds} . It takes, respectively, about 11.4 and 12.2 time units for the fastest particles released at the control and sensor location to reach m ; for this reason, n_{du} and n_{ds} are set to the corresponding values of $n_{du} = 114$ and $n_{ds} = 122$ (since $dt_m = 0.1$). The n_{du} coefficient

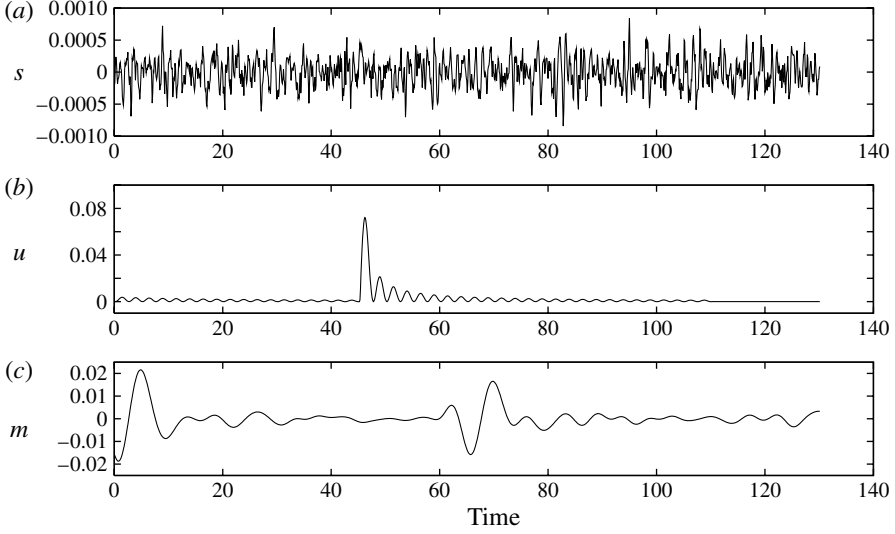


FIGURE 6. Three alternative data sequences, that define the first testing dataset (a) the measurement s capturing the influence of external noise, (b) a deterministic, broadband control law u , (c) the measurement m taken near the reattachment point.

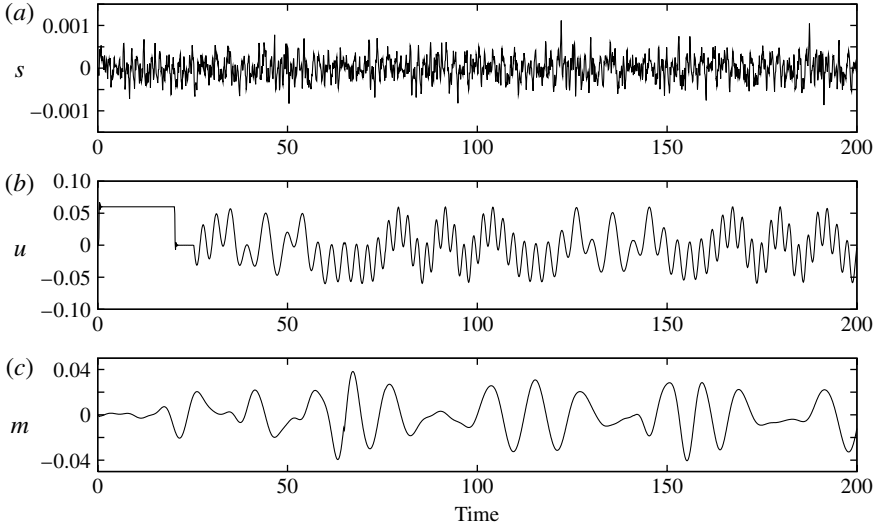


FIGURE 7. Three alternative data sequences, that define the second testing dataset (a) the measurement s capturing the influence of external noise, (b) a deterministic, broadband control law u , (c) the measurement m taken near the reattachment point.

is consistent with the value we found by evaluating the cross-correlation between u and m .

The coefficient n_{bu} is set to 49 such that the first visible peak in figure 8(b) is captured. We therefore set $n_{bs} = n_{bu} = 49$. Numerical tests revealed that the model showed little sensitivity to variations in the coefficients $[n_{bu}, n_{bs}]$. The grey zone

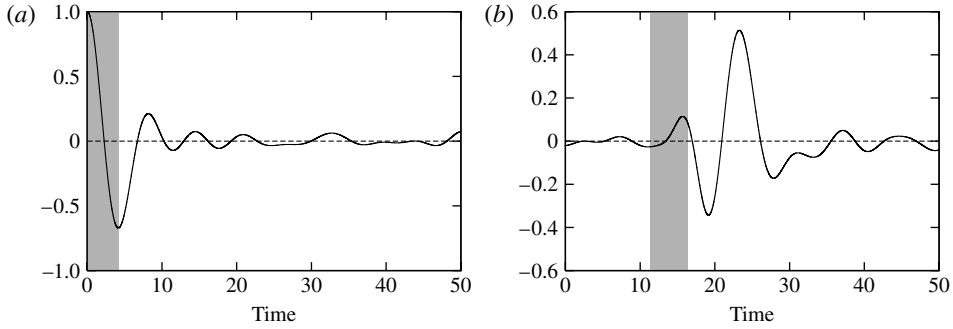


FIGURE 8. Correlations between temporal signals: (a) auto-correlation of m and (b) cross-correlation between u and m . The shaded area indicates the window length that is relevant for the proper performance of the auto-regressive model.

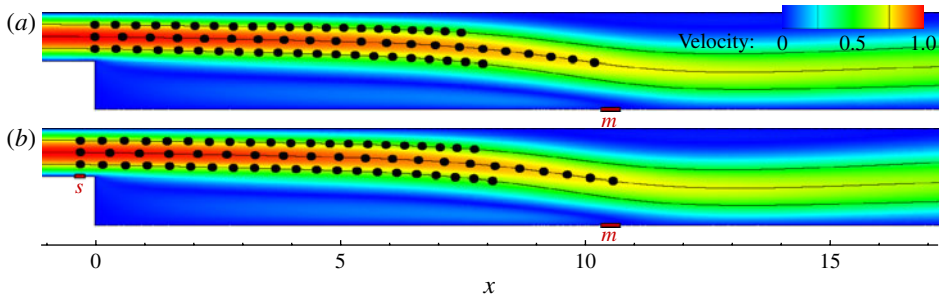


FIGURE 9. Motion along the base flow streamlines. (a) from $t = 0$ to $t = 11.4$, starting at the location of the controller. (b) $t = 0$ to $t = 12.2$, starting at the location of the upstream sensor. The contours are coloured according to the base flow velocity.

in figure 8(b) is bounded by $t/dt_m = [n_{du}; n_u]$. We recall that it is not necessary to increase n_{bu} in order to obtain an efficient model; a signal that is sufficiently auto-correlated can be represented with only a few coefficients b_k by using an auto-regressive equation (see the arguments in §4.1.1). The chosen grey zone contains the first arrival of information from u in the measurement m . An alternative, direct identification of the Markov parameters (that is, by setting $n_a = 0$) is conceivable but, in this case, the coefficient n_u should be set to at least $n_u = 300$. This value stems from the approximate support of the signal in figure 8(b), yielding a state–space model more than doubled in size. This exercise highlights the importance of the auto-regressive part of the model which is able to capture the dynamics in a far more compact manner.

Finally, the coefficient n_c can simply be chosen by evaluating various models once the remaining coefficients have been determined. By increasing n_c from 0 to 20, an optimal value at $n_c = 9$ has been found that resulted in very satisfactory results.

In summary, the selected values for the ARMAX coefficients can be found in table 2.

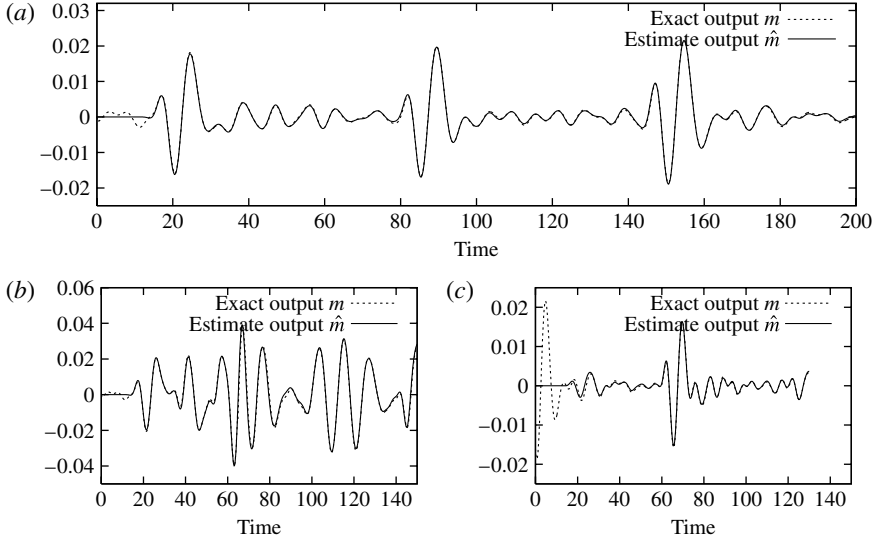


FIGURE 10. Performance of the system-identified model ARMAX_0 compared to DNS measurements. The ARMAX model starts from the zero state, and results are compared to the DNS dataset: (a) learning dataset; (b) validation dataset 1; (c) validation dataset 2 .

n_a	n_{bu}	n_{bs}	n_{du}	n_{ds}	n_c
36	49	49	114	122	9

TABLE 2. Choice of coefficient values for the ARMAX model.

4.2.3. Identification algorithm

The computation of an ARMAX model (with $n_c > 0$) involves an iterative algorithm. Owing to the non-white-in-time error term E , the algorithm can ensure stability by modelling the unpredictable dynamics as the error. We used the MatLab routine `armax` to compute the model; more details about the algorithm can be found in Ljung (1999).

4.2.4. Model performance

Figure 10 illustrates the performance of the system-identified ARMAX model, in particular its accuracy in reproducing the output m for the three datasets displayed in figures 4, 6 and 7. The model is based on the ARMAX equation (4.1), whose coefficients are listed in table 2. In what follows, this model will be referred to as ARMAX_0 ; it estimates the output m from the inputs u and s . The identified model is initialized with a zero state vector (which explains the vanishing values for $t \in [0 \ 11.4] = [0 \ n_{du}]dt_m$) and is only driven by (s, u) to provide an estimate for m . The output of the model is compared to the measurement m from DNS: the model is able to predict the output with very high accuracy, which validates both the relevance of the model equation (4.1) and the implementation of the s -sensor to provide important information to the model.

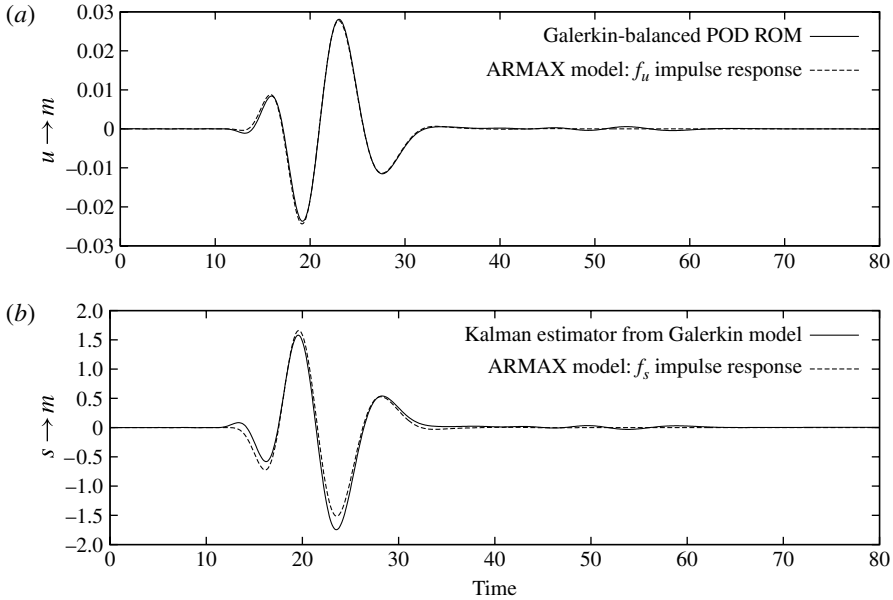


FIGURE 11. Galerkin-based ROM versus ARMAX impulse responses. (a) From u to m .
(b) From s to m .

4.3. Comparison between Galerkin-POD and ARMAX model

For the sake of completeness, a comparison between the identified model and a Galerkin-based model is presented. As mentioned in § 3, both the Galerkin-based Kalman filter (3.2) and the system-identified model (4.1) aim at presenting the output m as a function of the two inputs u and s . In addition, both models are linear and can thus be compared using their respective impulse response. To this end, we computed a Galerkin reduced-order model, taking advantage of full knowledge of our numerical system (note that the computation of the Galerkin ROM cannot be performed within the pseudo-experimental setup introduced in § 3.2.2).

We proceeded as described in Rowley (2005). First, two snapshot sequences for the impulse responses of the direct equations starting with an impulse in u , and w are computed which are then used to determine a balanced-POD basis that was thereafter truncated to contain 23 modes. The Navier–Stokes equations are then projected onto this truncated basis. A Kalman estimator is then computed to estimate the state from upstream measurements s . As we do not consider sensor noise in this section, the Kalman filter is computed in the large-gain limit (which is equivalent to assuming $\text{var}(w) \gg \text{var}(g_s)$ in (3.1)). Solving an algebraic Riccati equation finally provides the Kalman filter (3.2), whose transfer functions correspond to (f_u, f_s) .

The Kalman estimator is known to be the optimal linear system that predicts the output measurement m given the inputs (u, s) . One can therefore expect the transfer functions of such a model to match the transfer functions obtained via ARMAX identification. Comparing the impulse response of different systems is therefore an appropriate test as it is independent of the chosen basis and the particular formulation of the model (state–space form or polynomial representation of the transfer function).

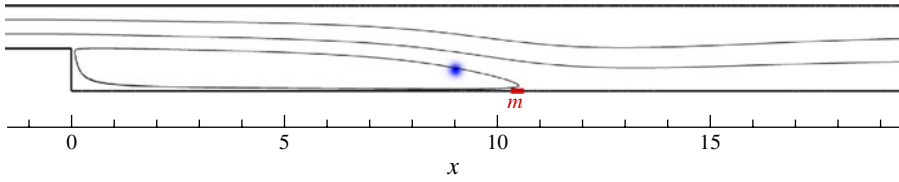


FIGURE 12. (Colour online) Additional source of noise. A Gaussian momentum forcing is located in the shear layer, near the end of the recirculation bubble so that it generates structures that impact on m but not s .

	\underline{x}_0	\underline{y}_0	$\underline{\sigma}_x$	$\underline{\sigma}_y$	\underline{A}
Additional noise	9	-0.5	0.1	0.1	7.2

TABLE 3. Parameters that define the spatial Gaussian distributions of the new noise source. It is located in the shear layer, near the end of the recirculation bubble so that it will create structures that impact on m but not s .

Figure 11 shows a comparison of the impulse responses that have been obtained using the Galerkin framework and using the ARMAX identification technique. It shows a remarkable correspondence between the two models, which again corroborates the ability of the chosen system-identification technique to capture the relevant flow dynamics.

4.4. Robustness of the ARMAX model with respect to non-predictable forcing sources

In a realistic environment, the external disturbances may arise from multiple locations, and some of them may not be observable by the upstream sensor. Nevertheless, they can influence the output m and consequently disturb the identification process. In this section we investigate the effects of such perturbations on the identification process.

To highlight the properties of the ARMAX model, the results will be compared with those of purely linear models: an ARX model and a subspace model. The ARX model represents a special case of an ARMAX model with $n_c = 0$, whereas the subspace model is obtained as described in Huang & Kim (2008), with a dimension of 120. To model an unknown external excitation that impacts on the downstream sensor m without being observable by s , a new random forcing source is added to the flow: it is located in the shear layer, near the end of the recirculation bubble, so that it will impact on m without being detected by s . Figure 12 shows the precise location of the additional forcing source; numerically, it is modelled as a momentum forcing, similarly to the main forcing source (the coefficients are given in table 3).

In such a configuration, the downstream sensor measures the combination of *predictable dynamics* (by s) that arise from the main forcing source and *unpredictable dynamics* that arise from the new forcing source. Ideally, the identified model should treat the unpredictable dynamics as the model error $E(t)$ (as introduced in § 3.2). In other words, it should ignore it and, rather, focus on the predictable dynamics whose effects can be cancelled by the controller. As far the controller is concerned, the objective is to attenuate the predictable noise, since the unpredictable part is out of reach.

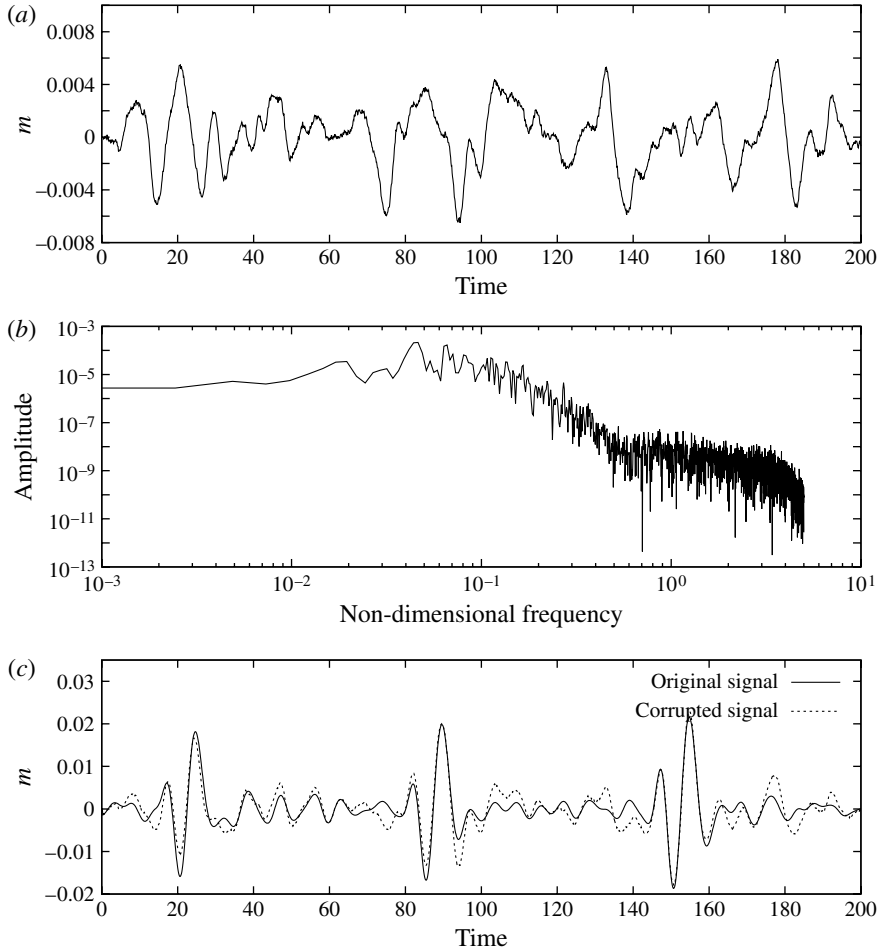


FIGURE 13. Additional source of noise: (a) signal generated by the additional forcing source alone; (b) periodogram of the perturbation signal; (c) resulting corrupted output signal, compared to the original (uncontaminated) signal.

As previously mentioned (see § 4.1.2), most linear system-identification techniques treat the model error as white noise; the ARMAX equation differs in this respect by allowing time-coloured noise. This additional feature is critically important in this study: the model error is certainly time coloured since it corresponds to physical structures that do not affect s but are nonetheless advected and filtered by the flow until they eventually reach the sensor m .

Figure 13 displays the additional measurement (a), its power spectrum (b), as well as the resulting corrupted learning dataset (c). In figure 13(b) one can clearly see that the high frequencies are filtered by the flow before the excitations affect the output measurement. The standard deviation of the perturbation signal (figure 13a) is equal to 44% of the standard deviation of the original signal. New models are then obtained based on the corrupted dataset of figure 13(c). This is followed by simulations using the validation dataset of figure 6, which has not been corrupted by the

Presence of additional external forcing source:	No (%)	Yes (%)	Relative loss (%)
ARMAX fit	96	82	15
ARX fit	72	33	41
Subspace fit	95	49	48
Relative improvement from ARX to ARMAX	32	148	

TABLE 4. Influence of an additional external forcing on the ARX, subspace, and ARMAX model performance. While the ARMAX identification remains accurate in the presence of unpredictable forcing sources, the purely linear ARX and subspace models show a significant loss in performance.

additional forcing source; it is thus possible to compare the results obtained to those in § 4.2.4.

For a quantitative comparison, we use as a criterion the fraction of the output variation that is captured by each model. We introduce

$$\text{fit} = 1 - \frac{\|m_{\text{simulated}} - m_{\text{ref}}\|}{\|m_{\text{ref}} - \text{mean}(m_{\text{ref}})\|}. \quad (4.8)$$

For the regression of the ARX and ARMAX models, we use the same coefficients as those given in table 2, except for n_c . Owing to the dependence of the ARMAX model on the properties of the unpredictable noise, the value of n_c had to be adjusted. As in § 4.2.2, n_c has been varied from 0 to 20, and best results have been obtained for $n_c = 17$.

Figure 14 depicts the performance of the ARX, subspace, and ARMAX models in recovering the (clean) validation dataset, with an additional source of noise having been present during the identification process. Both purely linear models show inferior performance, while the ARMAX model performs well in predicting both the control peak response and the subsequent dynamics. Quantitative results are given in table 4. For comparison, we also conducted tests using the initial (uncorrupted) learning dataset of figure 4 during the identification process; results are also given in table 4 (column headed No). In the presence of *mostly predictable* dynamics, the ARX performance is significantly lower than the subspace model performance; the latter is comparable to ARMAX. This is consistent with the results of Huang & Kim (2008) where the subspace model showed better performance than the ARX model. On the other hand, both purely linear models suffer a severe loss in performance when the identification processes are afflicted by unpredictable time-coloured noise. The ARMAX model, on the other hand, fared significantly better, which underlines the importance of the moving-average component of the model to cope with unpredictable dynamics in the flow.

5. Feed-forward control

In this section, we build a compensator based on the ARMAX₀ model. It consists of a dynamical linear system that is designed to compute an optimal control law u from the measured signal s . The objective of the controller is to minimize the quadratic norm of the measurement m . The control design is detailed in § 5.1, before the compensator is used to control the direct numerical simulation in § 5.2.

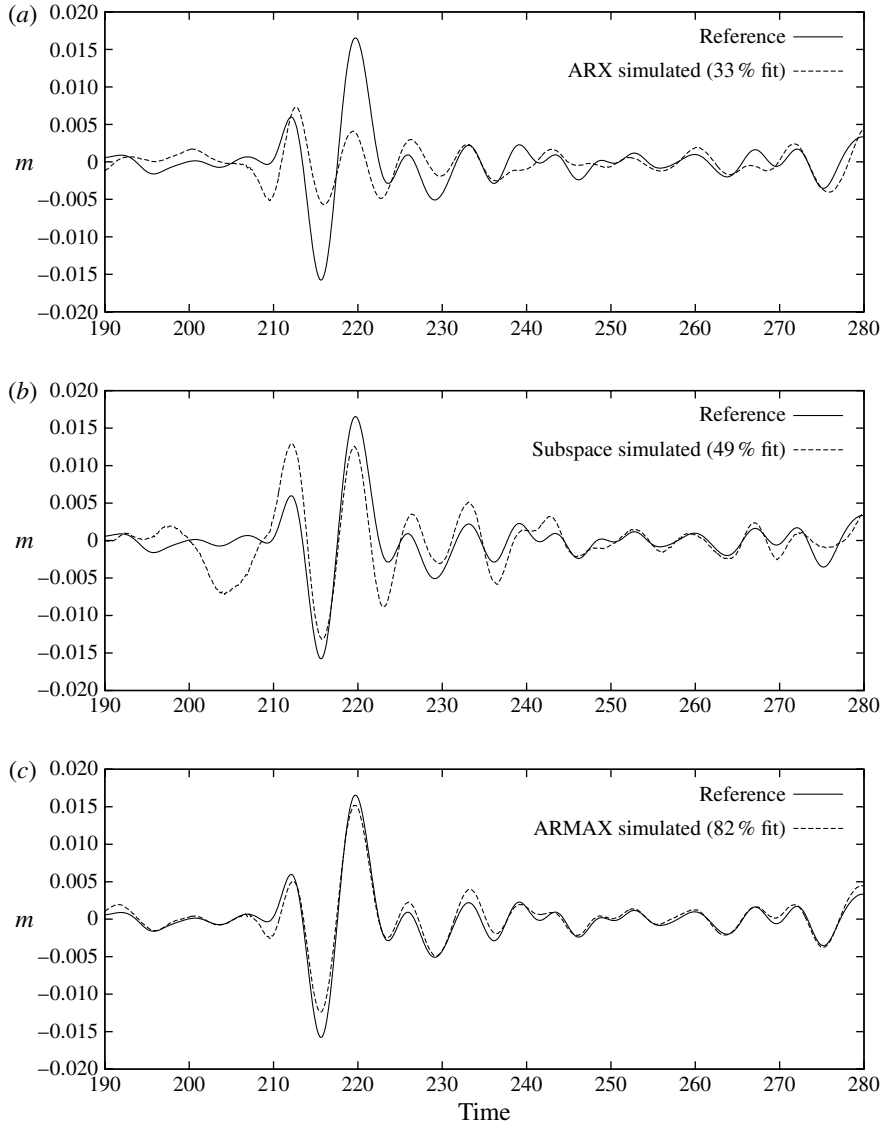


FIGURE 14. Comparison of the performance of (a) ARX, (b) subspace and (c) ARMAX models to recover the validation dataset. The models were identified in the presence of an unpredictable noise source. Both purely linear models are substantially affected by the presence of time-coloured noise, and do not provide accurate estimations of the signal. The ARMAX model, on the other hand, remains accurate despite a small loss in performance. Note that the fit coefficient, defined in (4.8), has been computed using a longer simulation.

5.1. Control design

Considering (3.4a), together with the objective to minimize $\|m\|$, the control law may formally be written as

$$u = -f_u^{-1}f_s s. \tag{5.1}$$

In practice, f_u cannot be properly inverted, and a pseudo-inverse has to be used. This consists of finding a control vector that minimizes the prediction of the output m , from t to $t + T$ where T defines the control horizon (whose value will be set below).

5.1.1. Designing the compensator dynamics

Using the impulse responses f_u and f_s displayed in figure 11, one can construct the two Markov sequences defined in (4.2). Figure 11 shows that both impulse responses eventually converge towards zero, which justifies our assumption of $h_{k>500=N_0} = 0$ (the index N_0 corresponds to a time $t = 50$). For an arbitrary discrete-time control horizon $T > N_0$, the output measurement vector \mathbf{M}_T that results from a combination of a past control vector \mathbf{U}^p , a future control vector \mathbf{U}^f and a past measurement vector \mathbf{S}^p reads

$$\underbrace{\begin{pmatrix} m_t \\ m_{t+1} \\ \vdots \\ m_{t+T} \end{pmatrix}}_{\mathbf{M}_T} = \underbrace{\begin{pmatrix} h_0^u & & & \\ h_1^u & h_0^u & & \\ \dots & & \ddots & \\ h_T^u & \dots & & h_0^u \end{pmatrix}}_{\mathbf{H}_u} \underbrace{\begin{pmatrix} u_t \\ u_{t+1} \\ \vdots \\ u_{t+T} \end{pmatrix}}_{\mathbf{U}^f} + \underbrace{\begin{pmatrix} h_1^u & \dots & & h_T^u \\ h_2^u & \dots & h_T^u & 0 \\ & \ddots & & \\ h_T^u & \dots & & 0 \\ 0 & \dots & \dots & 0 \end{pmatrix}}_{\mathbf{G}_u} \underbrace{\begin{pmatrix} u_{t-1} \\ u_{t-2} \\ \vdots \\ u_{t-T} \end{pmatrix}}_{\mathbf{U}^p} \\ + \underbrace{\begin{pmatrix} h_0^s & \dots & & h_T^s \\ h_1^s & \dots & h_T^s & 0 \\ & \ddots & & \\ h_T^s & \dots & & 0 \end{pmatrix}}_{\mathbf{G}_s} \underbrace{\begin{pmatrix} s_t \\ s_{t-1} \\ \vdots \\ s_{t-T} \end{pmatrix}}_{\mathbf{S}^p}. \quad (5.2)$$

To define the compensator, we minimize the predicted output norm $\|\mathbf{M}_T\|_2^2$. The solution then reads

$$\mathbf{U}^f = (-\mathbf{H}_u^+ \mathbf{G}_u) \mathbf{U}^p + (-\mathbf{H}_u^+ \mathbf{G}_s) \mathbf{S}^p, \quad (5.3a)$$

$$u(t) = \begin{bmatrix} 1 & 0 & \dots & 0 \end{bmatrix} \mathbf{U}^f, \quad (5.3b)$$

where \mathbf{H}_u^+ denotes the pseudo-inverse of \mathbf{H}_u (Penrose 1955). Equation (5.3) defines a linear dynamical system, whose inputs are the past measurements s and the past control inputs u , and whose output is $u(t)$. In practice, using a simple inverse would provide a system where the high frequencies are highly amplified, since $f_u \rightarrow 0$ at high frequencies. A pseudo-inverse is required with a non-zero tolerance level; it is based on the reciprocals of all singular values of \mathbf{H}_u that fall above a user-specified threshold. Setting this tolerance level is equivalent to applying a filter and enables an effective compensator design. Regardless of the tolerance level, the performance of the compensator increases with T . We set $T = 1000$, which corresponds to a non-dimensional time length of $t = 100$. For the tolerance level, best results were obtained for a value of 0.0218, where 48 singular values are retained.

5.1.2. Balanced truncation and characterization of the compensator

Once the compensator has been designed, it can be recast into a simpler state-space model through balanced truncation (the algorithm is described in Safonov & Chiang 1989). The transfer function of the compensator (5.3) can be described, without significant loss in accuracy, by a 14-modes state-space model that reads, in general

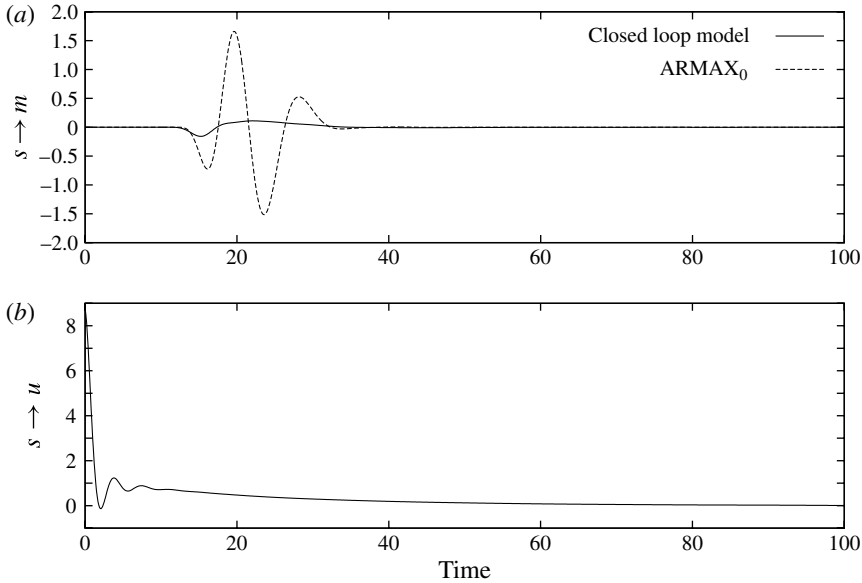


FIGURE 15. Impulse response of both the open-loop and closed-loop models. (a) Predicted measurements. The response of ARMAX₀ is the same as in figure 11. (b) Control law (corresponds to the impulse response of the compensator). Closing the loop efficiently reduces the effects of an impulse in s for the model.

form,

$$\mathbf{X}(t+1) = \mathbf{A}\mathbf{X}(t) + \mathbf{B}s(t), \quad (5.4a)$$

$$u(t) = \mathbf{C}\mathbf{X}(t) + \mathbf{D}s(t). \quad (5.4b)$$

Figure 15(a) shows a comparison between the impulse response of the open-loop model (no control) and impulse response of the closed-loop model (where the compensator is used to provide the control law). As expected, it shows a very effective reduction of the predicted output. The associated control law is shown in figure 15(b).

5.2. Control results

5.2.1. Using perfect sensors

So far, the effectiveness of the compensator has been tested on the identified model ARMAX₀ itself. In this section, we present results from DNS as the control. The compensator is driven by measurements from the DNS; the DNS, in turn, uses the control law that the compensator provides. The time step for the compensator has been changed from dt_m to dt_{dns} in order to compute a control law at each time step of the DNS while keeping the same transfer function. Such a transformation is straightforward and described in Antoulas (2005).

Figures 16 and 17 show the control performance using a compensator that consists of a state–space system of 14 modes. As anticipated, the compensator not only reduces the fluctuations of m (the r.m.s. value of the output fluctuations is reduced by 93% in figure 16) but also accomplishes a reduction of 99% of the perturbation energy in the entire computational domain (figure 17).

Figure 18 depicts the average turbulent kinetic energy of both the uncontrolled and the controlled simulations. The maximum peak of turbulent energy is located at

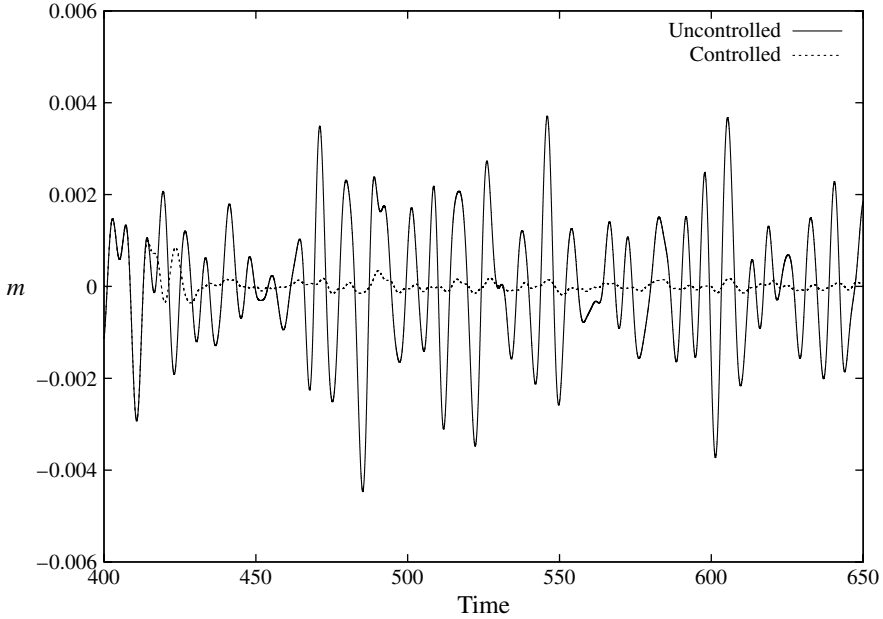


FIGURE 16. Output measurement m extracted from the DNS as a function of time. Both the controlled and the uncontrolled simulations (using the same exact source of random noise) are compared. The compensator is based on 14 modes, and the sensors are taken as noise-free.

$x \approx 25$ in both cases, with the output sensor placed near the reattachment point of the separation bubble (at $x = 10.5$). The maximum peak of turbulent energy coincides with the location where the convective instability ends, which is in agreement with linear theory. The choice of the downstream skin-friction measurement m as an appropriate objective for the control design is validated, since the reduction of its fluctuations led to a substantial reduction of the turbulent energy in the entire computational domain. The turbulent kinetic energy is reduced by 96 % at $x \approx 25$, the same location as where the uncontrolled turbulent kinetic energy is maximal.

5.2.2. Using noisy sensors

Noisy sensors are modelled by adding white Gaussian noise to all measured signals. Noise on m only affects the design process, whereas a noisy measurement s affects both the design process and the compensated simulation (the compensator is driven with a noise-contaminated measurement).

Figures 19 and 20 display the difference between the exact and corrupted signals, both for m and s , for different standard deviations of the noise. The noise root-mean-square (r.m.s.) value is expressed as a percentage of the r.m.s.-value of the exact signal. The same learning dataset has been used and corrupted with different levels of measurement noise. All models are generated using the same coefficients n_a , n_{bu} , n_{bs} , n_{du} , n_{ds} , n_c and the same tolerance for the pseudo-inverse.

Figure 21 illustrates the effect of the measurement noise on the control performance. The energy of the fluctuations is plotted versus time for the various simulations, and the standard deviation of the noise measurements is expressed as a percentage of the r.m.s. value of the noise-free signal. The compensator appears to be quite robust to measurement noise and remains effective even with the two measurements $[s, m]$

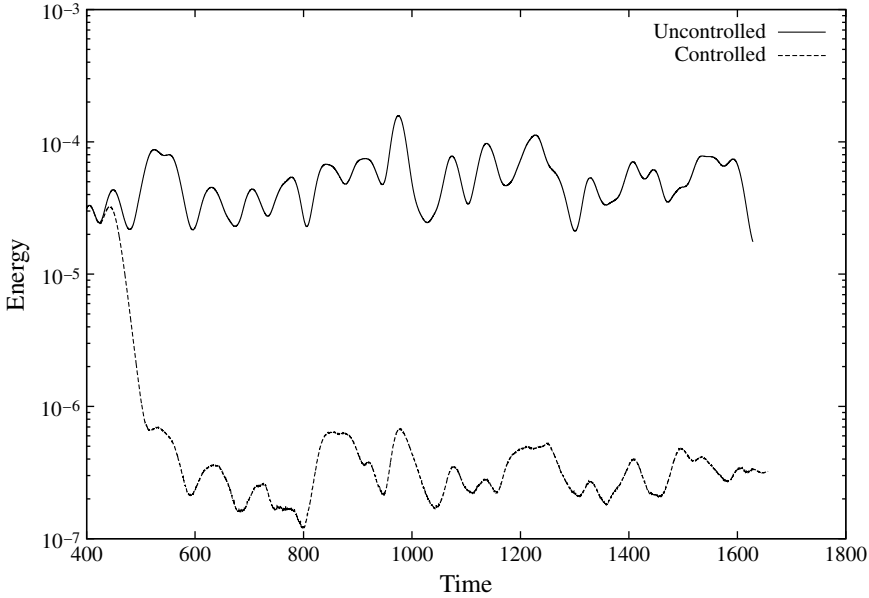


FIGURE 17. Perturbation energy from the DNS as a function of time. Both the controlled and the uncontrolled simulations (using the same exact source of random noise) are compared. The compensator is based on 14 modes, and the sensors are taken as noise-free.

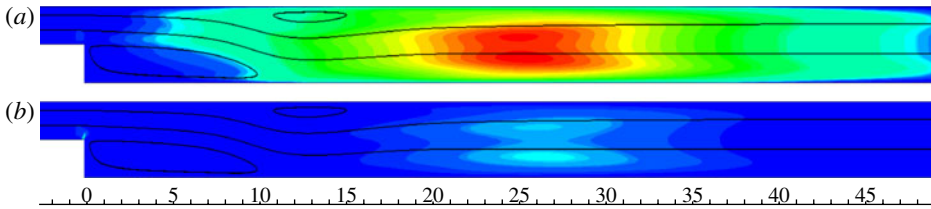


FIGURE 18. Contours of the mean turbulent kinetic energy from the numerical simulation (the vertical coordinate is stretched for more clarity). (a) Uncontrolled simulation. (b) Controlled simulation. Streamlines of the base flow are also shown. The control action is barely visible at the top corner of the step in the controlled simulation. The maximum peak of turbulent kinetic energy is reduced by 96%.

corrupted by 100% of their respective signal-r.m.s. As expected, noise-corrupted measurements, in general, lead to a reduced control performance. More specifically, a contamination of the signal s shows more effect on the performance than an equal contamination of the signal m . This should not come as a surprise since the measurement noise g_m is eliminated during the ARMAX regression and thus never appears again. A corruption of the measurement s , on the contrary, will affect both the ARMAX regression and the input signal of the compensator.

5.2.3. Using stronger perturbations

As the noise levels are raised, nonlinear effects start to come into play during the numerical simulations. To facilitate a comparison, the same random source sequence is used but is simply multiplied by a different amplitude $\underline{\sigma}_w$ (see table 5). The

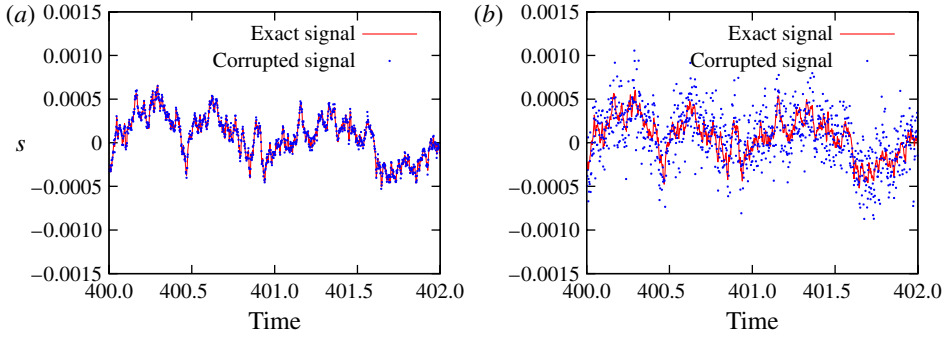


FIGURE 19. Short sequence of the noisy signal s , corrupted by 10 % of the r.m.s. of s (a) and by 100 % of the r.m.s. of s (b). The exact signal is extracted from the controlled numerical simulation whose energy is shown in figure 17.

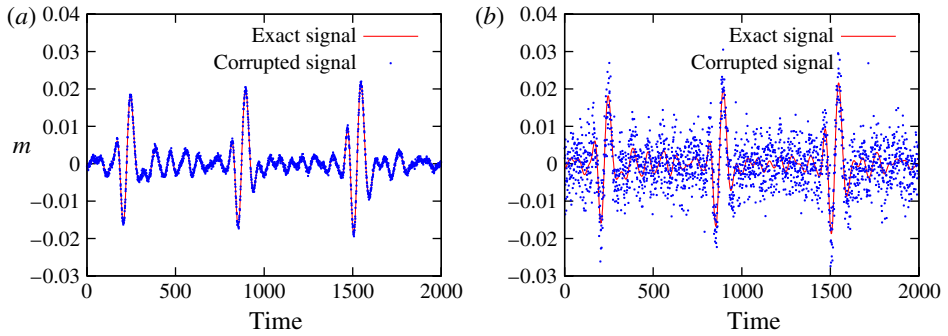


FIGURE 20. Comparison between the noise-free and noisy signal m from the learning dataset: (a) corrupted by 10 % of the r.m.s. of m , (b) corrupted by 100 % of the r.m.s. of m .

	n_1	n_2	n_3	n_4	n_5	n_6	nl_1	nl_2	nl_3
m_{rms} reduction (in %)									
Achieved	93	75	66	42	22	15	93	80	23
Expected	93	75	69	37	22	18	—	—	—
Energy reduction (in %)									
Achieved	99	95	85	76	55	43	98	87	49
Standard deviation of the noise σ_w	0.01	0.01	0.01	0.01	0.01	0.01	1	$\sqrt{10}$	10

TABLE 5. Summary of achieved and expected controller performances, as well as model-expected performances. n_i refers to the simulations from § 5.2.2 probing the influence of measurement noise; nl_i refers to the simulations from § 5.2.3 assessing the effects of nonlinearities. The relative standard deviation of the noise in the DNS computation is given by σ_w .

same controller based on ARMAX_0 (which has been computed with $\underline{\mathbf{G}}_s = \underline{\mathbf{G}}_m = 0$ and $\sigma_w = 0.01$) is used for each simulation. To quantify the amount of nonlinear

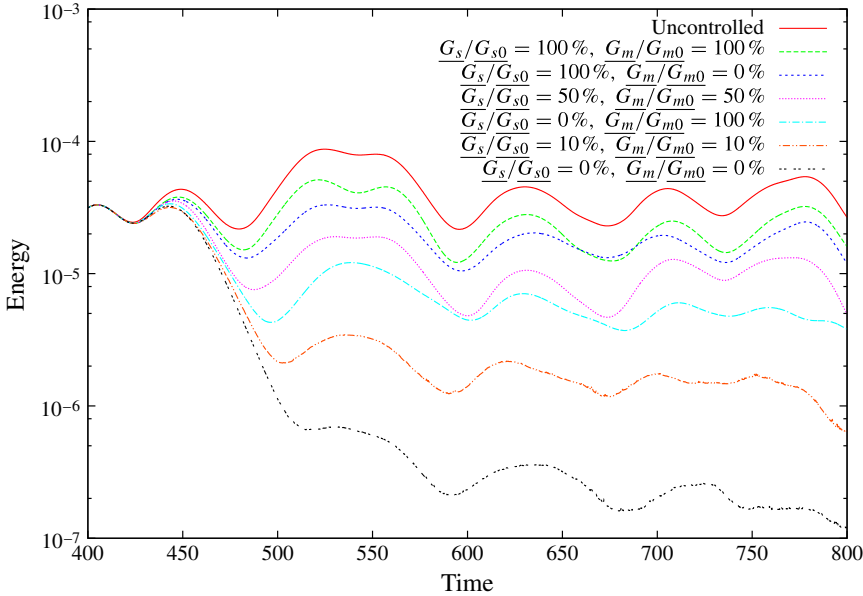


FIGURE 21. Effect of noisy sensors on the overall controller performance, measured by the kinetic energy (in semilog scale) versus time. Noise levels are expressed in percentage of the r.m.s. of the exact signals.

effects, a linearized simulation based on the same random source sequence has been computed. Figure 22 shows the resulting energy plots where three levels of noise are presented. Each level is displayed in a different colour; the dashed lines show the energy of the uncontrolled simulation, while the solid lines correspond to the controlled simulations. Symbols correspond to the extrapolated linear uncontrolled simulation, so that the difference between symbols and dashed lines shows the effects of nonlinearities. In each case, the controller starts at $t = 100$. For each simulation, the controller accomplishes a reduction of the perturbation energy. However, the *relative* energy reduction diminishes as the noise amplitudes (and thus the nonlinear effects) increase.

Figure 23 shows the average turbulent kinetic energy of the uncontrolled and controlled simulations for the case with strongest noise levels (the pink lines in figure 22). Compared to the linear case, the maximum peak of the turbulent energy has shifted to $x \approx 8$, a manifestation of the linear theory no longer holding. Nevertheless, the controller has been able to reduce the maximum peak of turbulent kinetic energy by an impressive 88 % (the maximum energy peak values for uncontrolled/controlled simulations are taken at $x \approx 8$ and $x \approx 15$, respectively) whereas the global reduction is 49 % (see nl_3 in table 5).

5.2.4. A final comparison

Table 5 summarizes the results of different controlled simulations. The abbreviations n_1, \dots, n_6 correspond to the six simulations performed in § 5.2.2 (see figure 21), arranged in descending order of energy reduction. The abbreviations nl_1, \dots, nl_3 correspond to the simulations that have been shown in § 5.2.3, figure 22, sorted in the same way. The expected reduction in the r.m.s.-values of m originates from the

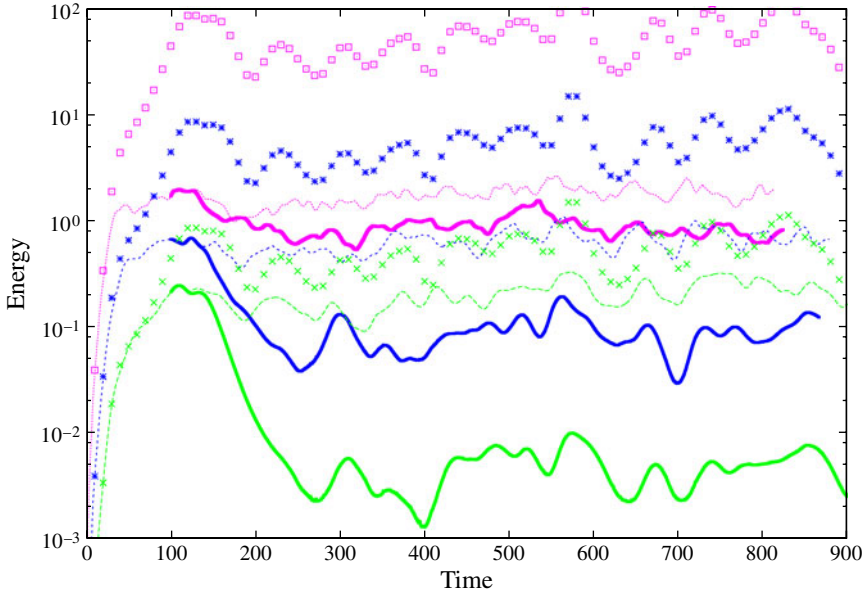


FIGURE 22. Control of nonlinear flows, displayed by perturbation energy as a function of time. Dashed lines: uncontrolled nonlinear simulations; solid lines: controlled nonlinear simulations. Symbols: extrapolated linear simulation. Curves of the same colour correspond to same level of noise excitation in the uncontrolled DNS. The controller starts after an initial transient period at $t = 100$.

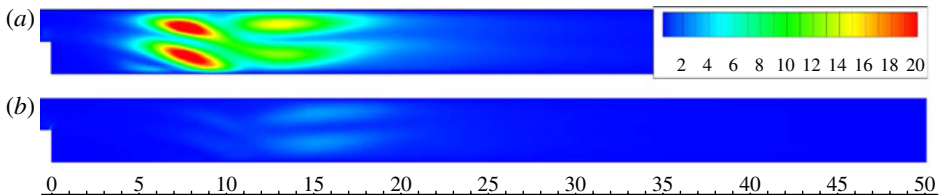


FIGURE 23. Contours of the average turbulent kinetic energy ($v_x^2 + v_y^2$) from the nonlinear numerical simulations (the vertical scale is stretched for more clarity). (a) The uncontrolled simulation; (b) the controlled simulation. The maximum peak of uncontrolled mean turbulent kinetic energy is located at $x \approx 8$ and is reduced through control efforts by 88%.

control of the specific model that has been computed in § 4.2 by assuming noise-free sensors and low levels of environmental noise.

6. Conclusions

The flow over a backward-facing step has been considered as a typical amplifier flow where the influence of noise sources and model uncertainty plays a dominant role in the design of accurate low-order models and effective controllers. This type of flow is often encountered in industrial settings and research experiments; model-based control strategies, however, have shown only limited success when applied to amplifier flows under realistic disturbance environments. Rather than enforcing a particular

(idealized) flow model *a priori*, a model is extracted directly from time sequences of observable data. During the design process, special care has to be taken that only data which are readily available, e.g. in an experiment (generally contaminated by noise), enter the system-identification procedure.

In our case, a model has been designed based on an ARMAX-equation which consists of an auto-regressive (AR) component for the measurements, a moving-average (MA) component for the collective noise sources, and exogenous (X) terms for the input variables. The latter input variables are composed of the control input as well as an upstream sensor signal which acts as a proxy variable for the unknown upstream noise. The coefficients of this regression model are chosen on physical grounds by considering the general convective behaviour of the flow for the delay terms and by analysing the mutual influence (or lack thereof) of actuators and sensors. In a second step, the model forms the base of a feed-forward controller. Applying this combined system-identification/control-design approach to our flow over a backward-facing step yielded remarkable results. A reduction of more than 90% of the measurement energy and total energy could be observed. Increasing the noise levels to high values did not compromise the stability of the compensator, even though its effectiveness diminished accordingly. An application of the linearly designed compensator to a nonlinear numerical simulation showed encouraging results. The *total* turbulent kinetic energy could still be reduced by nearly 50% and the *maximal* turbulent kinetic energy by 88%, even though the compensator operated far off its design point.

In summary, a robust and compelling flow control procedure has been introduced that is data-based in the model design and follows classical methods for model-reduction and control layout. This technique is particularly attractive for amplifier flows, where the accurate modelling of noise sources and their influence on system dynamics and sensor output is imperative for a successful compensator performance. It should also appeal to experimental efforts and practical applications of closed-loop flow control.

REFERENCES

- AKERS, J. C. & BERNSTEIN, D. S. 1997 ARMARKOV least-squares identification. *Proc. Am. Contr. Conf.* 186–190.
- AKERVIK, E., HOEPFNER, J., EHRENSTEIN, U. & HENNINGSON, D. S. 2007 Optimal growth, model reduction and control in a separated boundary-layer flow using global eigenmodes. *J. Fluid Mech.* **579**, 305–314.
- ANTOULAS, A. C. 2005 *Approximation of Large-Scale Dynamical Systems. Advances in Design and Control*, Society for Industrial and Applied Mathematics.
- BAGHERI, S., BRANDT, L. & HENNINGSON, D. S. 2009 Input/output analysis, model reduction and control of the flat-plate boundary layer. *J. Fluid Mech.* **620**, 263–298.
- BARBAGALLO, A., SIPP, D. & SCHMID, P. J. 2009 Closed-loop control of an open cavity flow using reduced-order models. *J. Fluid Mech.* **641**, 1–50.
- BARKLEY, D., GOMES, M. G. M. & HENDERSON, R. D. 2002 Three-dimensional instability in flow over a backward-facing step. *J. Fluid Mech.* **473**, 167–190.
- BLACKBURN, H. M., BARKLEY, D. & SHERWIN, S. J. 2008 Convective instability and transient growth in flow over a backward-facing step. *J. Fluid Mech.* **603**, 271–304.
- CATTAFESTA, L., WILLIAMS, D. R., ROWLEY, C. W. & ALVI, F. 2003 Review of active control of flow-induced cavity resonance. *AIAA Paper* 2003-3567.
- DERGHAM, G., SIPP, D. & ROBINET, J.-C. 2011 Accurate low dimensional models for deterministic fluid systems driven by uncertain forcing. *Phys. Fluids* **23** (9), 094101.
- EFE, M. O. & OZBAY, H. 2003 Proper orthogonal decomposition for reduced order modelling: 2D heat flow. *IEEE Conf. Contr. Appl.* **2**, 1273–1277.

- GIBSON, J. S., LEE, G. H. & WU, C. F. 2000 Least-squares estimation of input/output models for distributed linear systems in the presence of noise. *Automatica* **36** (10), 1427–1442.
- GLOWINSKI, R. 2003 Finite element methods for incompressible viscous flow. In *Handbook of Numerical Analysis* (ed. P. G. Ciarlet & J. L. Lions). *Numerical Methods for Fluids (Part 3)*, vol. 9. pp. 3–1176. Elsevier.
- HUANG, S.-C. & KIM, J. 2008 Control and system identification of a separated flow. *Phys. Fluids* **20** (10), 101509.
- JUANG, J. N. & PAPPAS, R. S. 1985 An eigensystem realization algorithm for modal parameter identification and model reduction (control systems design for large space structures). *J. Guid. Control Dyn.* **8**, 620–627.
- KIM, J. & BEWLEY, T. R. 2007 A linear systems approach to flow control. *Annu. Rev. Fluid Mech.* **39**, 383–417.
- LJUNG, L. 1999 *System Identification: Theory for the User*, 2nd edn. Prentice Hall.
- MA, Z., AHUJA, S. & ROWLEY, C. W. 2010 Reduced-order models for control of fluids using the eigensystem realization algorithm. *Theor. Comput. Fluid Dyn.* **25**, 1–15.
- MARQUET, O., SIPP, D., CHOMAZ, J.-M. & JACQUIN, L. 2008 Amplifier and resonator dynamics of a low-Reynolds-number recirculation bubble in a global framework. *J. Fluid Mech.* **605**, 429–443.
- MOORE, B. 1981 Principal component analysis in linear systems: Controllability, observability, and model reduction. *IEEE Trans. Autom. Control* **26** (1), 17–32.
- PENROSE, R. 1955 A generalized inverse for matrices. *Proc. Camb. Phil. Soc.* **51**, 406–413.
- ROWLEY, C. W. 2005 Model reduction for fluids, using balanced proper orthogonal decomposition. *Intl J. Bifurcation Chaos* **15** (5), 255–289.
- ROWLEY, C. W., COLONIUS, T. & MURRAY, R. M. 2004 Model reduction for compressible flows using POD and Galerkin projection. *Physica D* **189**, 115–129.
- SAFONOV, M. G. & CHIANG, R. Y. 1989 A Schur method for balanced-truncation model reduction. *IEEE Trans. Autom. Control* **34** (7), 729–733.
- SAMIMY, M., DEBIASI, M., CARABALLO, E., OZBAY, H., EFE, M. O., YUAN, X., DEBONIS, J. & MYATT, J. H. 2003 Development of closed-loop control for cavity flows. *AIAA Paper* 2003-4258.
- SAMIMY, M., DEBIASI, M., CARABALLO, E., SERRANI, A., YUAN, X., LITTLE, J. & MYATT, J. H. 2007 Feedback control of subsonic cavity flows using reduced-order models. *J. Fluid Mech.* **579**, 315–346.
- SIPP, D., MARQUET, O., MELIGA, P. & BARBAGALLO, A. 2010 Dynamics and control of global instabilities in open flows: a linearized approach. *Appl. Mech. Rev.* **63** (3), 030801.